Smyl, Danny; Bossuyt, Sven; Ahmad, Waqas; Vavilov, Anton; Liu, Dong

An overview of 38 least squares–based frameworks for structural damage tomography

Published in:
Structural Health Monitoring

DOI:
10.1177/1475921719841012

Published: 15/04/2019

Document Version
Peer-reviewed accepted author manuscript, also known as Final accepted manuscript or Post-print

Published under the following license:
Unspecified

Please cite the original version:
Smyl, D., Bossuyt, S., Ahmad, W., Vavilov, A., & Liu, D. (2019). An overview of 38 least squares–based frameworks for structural damage tomography. *Structural Health Monitoring*.
https://doi.org/10.1177/1475921719841012

An overview of 38 least squares–based frameworks for structural damage tomography

Article *in* Structural Health Monitoring · March 2019

DOI: 10.1177/1475921719841012

CITATIONS
0

READS
218

5 authors, including:

Danny Smyl
The University of Sheffield
25 PUBLICATIONS **96** CITATIONS
SEE PROFILE

Waqas Ahmad
Aalto University
1 PUBLICATION **0** CITATIONS
SEE PROFILE

Dong Liu
University of Science and Technology of China
31 PUBLICATIONS **151** CITATIONS
SEE PROFILE

Journal Title
XX(X):1–29

DOI: 10.1177/ToBeAssigned
www.sagepub.com/
SAGE

An overview of 38 least squares-based frameworks for structural damage tomography

Danny Smyl [1], Sven Bossuyt[2], Waqas Ahmad[2], Anton Vavilov[2], and Dong Liu[3]

Abstract

The ability to reliably detect damage and intercept deleterious processes, such as cracking, corrosion, and plasticity are central themes in structural health monitoring (SHM). The importance of detecting such processes early on lies in the realization that delays may decrease safety, increase long-term repair/retrofit costs, and degrade the overall user experience of civil infrastructure. Since real structures exist in more than one dimension, the detection of distributed damage processes also generally requires input data from more than one dimension. Often, however, interpretation of distributed data – alone – offers insufficient information. For this reason, engineers and researchers have become interested in stationary inverse methods, e.g. utilizing distributed data from stationary or quasi-stationary measurements, for tomographic imaging structures. Presently, however, there are barriers in implementing stationary inverse methods at the scale of built civil structures. Of these barriers, a lack of available straightforward inverse algorithms is at the forefront. To address this, we provide 38 least-squares frameworks encompassing single-state, two-state, and joint tomographic imaging of structural damage. These regimes are then applied to two emerging SHM imaging modalities: Electrical Resistance Tomography and Quasi-Static Elasticity Imaging. The feasibility of the regimes are then demonstrated using simulated and experimental data.

Keywords

Elasticity Imaging, Electrical Imaging, Inverse Problems, Structural Health Monitoring

Introduction

In recent years, the use of distributed data and full-field measurements have been the source of significant research interest in the field of structural health monitoring (SHM) (Farrar and Worden 2012; Ou and Li 2010; Balageas et al. 2010). Much of this interest is derived from the fact that full-field or distributed data offers increased spatial information relative to point data (Smyl et al. 2018c). While the use of distributed data does improve realizations related to structural state, inverse methods afford us additional quantitative information on structural state by incorporating *a priori* information in obtaining estimations of structural state from distributed data. Many forms of data are available to researchers, which are often used to generate images of structural damage, such as cracking, plasticity, impact, fatigue, and more. In particular, the use of photographic, piezoelectric, and electrical data have been used in inverse method-based applications within SHM.

The use of photographic data sets has shown promise in Digital Image Correlation (DIC) and Computer Vision based SHM. For in-plane imaging of plastic processes, DIC has proven to be a highly promising method – for which

[1]Department of Civil and Structural Engineering, The University of Sheffield, Sheffield, UK
[2]Department of Mechanical Engineering, Aalto University, Espoo, Finland
[3]Department of Modern Physics, University of Science and Technology of China (USTC), Hefei 230026, China

Corresponding author:
Danny Smyl, Dong Liu
Email: d.smyl@sheffield.ac.uk, dong2016@ustc.edu.cn

there are many available computational regimes (Pan et al. 2009). Some representative examples of DIC for SHM purposes include evaluation of crack propagation in concrete elements subject blast loading (Küntz et al. 2006), evaluation of interfacial debonding (Corr et al. 2007), and evaluation of microscopic strain and damage evolution in metals (Malitckii et al. 2018; Kang et al. 2007). Data sets generated from DIC have also been successfully used as input data for inverse regimes; in particular, Quasi-Static Elasticity Imaging (QSEI) which aims to reconstruct elastic properties from displacement fields (Smyl et al. 2018c). Computer Vision Techniques have also enjoyed much success in damage localization (Cha et al. 2017), identification of bolt loosening in steel structures (Kong and Li 2018a), and fatigue-crack detection (Kong and Li 2018b).

Implementation of piezoelectric sensors and actuators for lamb-wave based SHM has also been recognized as a promising method for detecting damage/defects in structural members. Researchers have demonstrated this in applications including defect detection in composite structures (Sohn et al. 2003; Paget et al. 2003), thin plates (Gangadharan et al. 2009), plates considering various deformation physics (Rose and Wang 2004), and a large suite of different problems. For this, a multitude of analytical, semi-analytical, and numerical approaches have been proposed (Park et al. 2007; Rose 2014).

Within only the past 8 years, the electrical data has proven successful in tomographic regimes for imaging spatially-distributed damage in structural members. Most often, researchers have been interested in imaging damage in concrete (Smyl et al. 2018d; Seppänen et al. 2014a; Hallaji et al. 2014) or composite structures (Tallman et al. 2017, 2015) by employing Electrical Resistance Tomography (ERT) – aiming to reconstruct the electrical conductivity from distributed voltage measurements. In concrete applications, aiming to detect discrete cracking, authors have utilized data obtained directly from the concrete surface (Karhunen et al. 2010) or from an electrically-conductive sensing skin (Seppänen et al. 2014b). In composite materials, often the material is self sensing (glass fiber/epoxy laminate) using electrically-conductive nanofillers. In both cases, ERT has been useful in applications from stain quantification to reconstructing complex cracking distributions in large area sensors.

With the possible exception of lamb-wave based SHM, the aforementioned examples may be used in *stationary* tomographic regimes aiming to reconstruct images of (potential) structural damage. This is in contrast to *nonstationary problems*, where we quote the description from Kaipio and Somersalo (Kaipio and Somersalo 2005).

> "In several applications, one encounters a situation in which measurements that constitute the data of an inverse problem are done in a nonstationary environment. More precisely, it may happen that the physical quantities that are the focus of our primary interest are time dependent and the measured data depends on these quantities at different times."

Moreover, the general use of stationary inverse problems for generating tomographic images of structural damage is a rather recent development, largely due to the computational demands in cases with many (roughly, greater than 10^3 (Oberai et al. 2003)) degrees of freedom. Examples of early applications include elasticity imaging (Bonnet and Constantinescu 2005), geometrical inverse problems using sensitivity analysis (Bonnet et al. 2002; Aithal and Saigal 1995), and general inverse problems employing boundary integral equations (Nishimura 1995; Mellings and Aliabadi 1995). More recently, researchers have taken advantage of rapidly improving computational resources by solving stationary SHM inverse problems ranging from approximately 10^4 (Yang et al. 2017; Gallo and Thostenson 2016; Dai et al. 2016) to more than 10^5 degrees of freedom (Zalameda et al. 2017; Smyl et al. 2017).

While considerable, computational challenges associated with implementing tomographic imaging within a SHM context is only one of many hurdles. In localizing and quantifying structural damage (such as a discrete crack), numerous considerations such as crack location, external loads, support conditions, and possibly most notably, structural size have significant impacts on acquired data and therefore the quantitative information obtained (Yao et al. 2014). To this end, the sheer ability to localize a crack using a tomographic modality is dependent on the input data being above some distinguishability criteria. If we choose, for example, the distinguishability criteria proposed by Isaacson (Isaacson 1986), we find that a crack is only detectable when two data sets D_1 (before damage) and D_2 (after damage) are above some measurement precision ε_m via a mean-squares criterion: $||D_2 - D_1|| > \varepsilon_m$. Practically speaking, measurement precision is only the theoretical distinguishability floor for damage detection; errors resulting from numerical modeling ε_n, discretization ε_d and sensor quality ε_s also contribute, resulting in a more realistic distinguishability criterion: $||D_2 - D_1|| > \varepsilon_m + \varepsilon_n + \varepsilon_d + \varepsilon_s$. These realizations imply a fundamental hurdle for implementing tomography for damage detection: that sufficiently small damage(s) may be undetectable (or, in the inverse problems sense, invisible (Greenleaf et al. 2009)).

In the context of damage tomography, the ability to even solve the intended computational inverse problem requires a numerical model for the underlying physics. Pragmatically speaking, no numerical method is completely accurate

(Surana and Reddy 2016; Oberkampf et al. 2002), resulting in ever-present uncertainty and modeling error ε_n. Broadly, there are four ways in dealing with ε_n: (i) ignore it, (ii) improve the numerical method, (iii) develop an approximation for ε_n (e.g., using subtraction (Seppänen et al. 2014a), the Bayesian approximation error approach (Nissinen et al. 2007), deep learning (Adler and Öktem 2017), etc.), and (iv) a combination of (ii) and (iii). In some cases, such as when structural damage processes are not significantly severe and/or complex, the use of (i) and (ii) may be sufficient (Smyl et al. 2018d); but, oftentimes, this is not true. The veiled need for (iii) in damage tomography may lie in the fact that damage in structures, either local or distributed, is notoriously nonlinear and difficult to model – although significant progress has been made in multi-scale numerical and constitutive modeling (LLorca et al. 2011; Nguyen et al. 2011; Liu and Zheng 2010).

Despite these ever-present practical challenges, we are inspired by the recent developments in stationary tomography of structural damage and increases in availability of computational resources which have helped to promote usage in SHM. At present, however, one barrier to the practical implementation of *stationary* tomography for SHM of built structures is the lack of availability of straightforward inverse frameworks and a transparent detailing of functionalities. In contrast, there is substantial literature detailing nonstationary inverse damage detection frameworks using vibration measurements (Wang and Chan 2009). These regimes have utilized, for example, natural frequency analysis (Moradi et al. 2011; Hejll 2004), modal displacement response (Zhang et al. 2013), modal strain energy (Cha and Buyukozturk 2015), changes in frequency (Salawu 1997), power spectrum (Gillich and Praisach 2014), and more. In solving these problems, algorithm complexity has ranged from advanced solution regimes including neural networks, genetic algorithms, particle swarm optimization, multi-objective function approaches, hybrid multi-objective approaches, and stochastic optimization approaches for non-convex problems (Jafarkhani and Masri 2011; Perera et al. 2010) to more basic regimes such as Finite Element updating, various gradient-based approaches, Newton methods, and quasi-Newton methods (Fan and Qiao 2011).

Possible explanations for the comparatively higher number of available vibration-based damage detection frameworks, with respect to stationary frameworks, results in part from factors discussed in the following. (a) The relative versatility in acquiring time-dependent data from accelerometers, laser systems, etc., whereas stationary tomography may require large-area sensors and/or advanced data acquisition systems posing practical challenges – a emerging topic that is currently the source of much research interest (Rashetnia et al. 2018). (b) The ability of vibration-based frameworks to meaningfully implement simple (e.g. one-dimensional) models in localizing damage (Reynders and De Roeck 2010). (c) The overall effectiveness of vibration-based methods for localizing damage. One potential advantage of stationary tomography in SHM is that it typically includes only a few data sets, therefore focus is often in promoting spatial resolution and accurately reconstructing damage geometry – these aims do not necessarily require large transfers of data or elegant optimization regimes. Rather, accomplishing these aims requires implementation of prior knowledge in regularization schemes, construction of noise models, appropriate use of error approximation methods, constrained optimization, and appropriate parameterizations that accurately represent the problem physics. The development of stationary inverse methods incorporating the aforementioned functionalities is a central theme of this article.

In this work, we focus on deriving and providing generic, adaptable, and straightforward regimes promoting improvements in spatial resolution and damage localization, which may be applied to a large suite of stationary inverse SHM problems. While this article is intended to serve as a primer for new users of stationary tomography in SHM. The article may also be a useful refresher to those who are already well-versed in inverse problems. For this, we derive a total of 38 least-squares frameworks for one state, two state, and joint tomographic imaging. Precisely, we aim to accomplish the following goals in this article:

- Derive one-state, two-state, and joint frameworks for stationary tomography of structural damage.
- Apply the frameworks to two promising SHM modalities: ERT and QSEI
- Demonstrate the frameworks' feasibility to image damage in structures using experimentally- and numerically-obtained data.

We note that, in this article, and in stationary tomographic applications in SHM in general, we are usually interested in fitting a computational model having n unknown parameters with m measurements (where $m > n$, making the system overdetermined). Broadly speaking, such a problem in SHM is referred to as a non-linear regression problem, meaning that the numerically-modeled data is non-linear in the unknown parameters and imposed conditions (such as boundary conditions, source terms, etc.) (Mueller and Siltanen 2012; Hartley 1961). In solving the non-linear regression problems, we utilize non-linear least squares approaches. This is done for three primary reasons, (i)

simplicity in implementation, (ii) ease of adaptability to include different regularization regimes and constraints, and (iii) rapid minimization.

At this point, it is apparent that the primary contribution of this article is the development and presentation of computational frameworks for structural damage tomography. With this in mind, it is important to place these aims in the context of inspection and monitoring processes. Overall, the frameworks provided in this article are intended to promote improved resolution and quantitative information on spatial structural damage processes. This task is iterative and computationally demanding, where the demand increases proportionally with the desired resolution and, roughly speaking, the size of the geometry investigated. As such, these frameworks are not presently intended for online monitoring processes. While this is a possible limitation in implementing the frameworks, there are also several promising avenues for utilization, such as, detection of damage processes not apparent or accessible via visual inspection, damage localization, remote detection of spatial damage processes, quantifying damage severity, quantifying spatial changes in damage over an inspection period, and incorporation of quantitative tomographic information into statistical models. To sum up, we strive to provide stationary tomography frameworks taking advantage of *a priori* knowledge to increase quantitative information on structural damage processes that may not be available through interpretation of data alone.

The paper is organized as follows. First, we provide a brief background on stationary inverse problems in the context of one-state problems. Following, we derive and provide frameworks (including cost functions and least squares solutions) for one state, two state, and joint tomography. Next, we integrate three different regularization schemes, constrained optimization, and (in the case of joint imaging) structural operators into the frameworks. We then, for clarity, provide as summary table including critical aspects for all the frameworks provided. Following, we apply selected frameworks to ERT and QSEI and provide examples testing the frameworks' feasibility. Next, a primer for first-time users of the damage tomography framework and recommendations/potential pitfalls in using the proposed frameworks are discussed. Lastly, conclusions are presented.

Stationary inverse problem frameworks

Single-state problems

The solution to a single-state stationary inverse problem involves estimating distributed parameters θ from data d. To do this, we generally aim to match some model U to the data by writing the observation model

$$d = U(\theta) \tag{1}$$

where U is called a *forward model*, usually solved computationally, for example by employing the finite difference or finite element method (Hansen 2005). The use of computational models in SHM applications is centered on the reality that structures may have arbitrary geometry, boundary conditions, and constitution – in such cases analytical or semi-analytical models are often not available. In an attempt to solve the basic problem posed in Eq. 1, we may aim to minimize a data discrepancy functional, such as

$$\Psi_1 = ||d - U(\theta)||^2 \tag{2}$$

where $||\cdot||$ is the Euclidean norm and the subscript "1" denotes the number of states considered. In general, however, solutions resulting from minimization of Eq. 2 may fail due to the ill-posed nature of the inverse problem, meaning that one of the following criteria is not satisfied: (i) a solution is unique, (ii) a solution exists, and (iii) the behavior of a solutions changes continually with the problem conditions (Kaipio and Somersalo 2005) (in other words, small changes in problem conditions/parameter values result in small changes in the solution – this is also known as the "stability" criterion). To handle the ill-posedness, we require regularization, which will be further detailed later. Moreover, the formulation of the problem in Eq. 2 is unrealistic, as any measured data contained some error e, which is commonly assumed to be Gaussian. Therefore, we re-derive the observation model by writing

$$d = U(\theta) + e. \tag{3}$$

In reality, additional sources of error also exist which add uncertainty to solutions of the inverse problem. A primary culprit is modeling error, i.e. errors in U that do not precisely match the problem physics (Surana and Reddy 2016). Such errors may be accounted for by adding a second error term in equation 3 using, for example Bayesian approximate error modeling (BAE) (Nissinen et al. 2007). In this work, however, we assume the modeling error as additive in the

term e to maintain simplicity in our regimes. We then aim to minimize the following functional in obtaining our inverse solutions

$$\Psi_1 = ||L_e(d - U(\theta))||^2 + \mathcal{R}(\theta) \tag{4}$$

where $\mathcal{R}(\theta)$ is a regularization functional and L_e is the Cholesky factor of the inverted noise covariance matrix W^{-1} (i.e. $L_e^T L_e = W^{-1}$). To obtain W, we have many options. Possibly the most convenient and robust methods include obtaining statistics by repeated measuring of a non-evolving structure or simply estimating W by trial and error (e.g. assume the measurement noise/errors are some small percentage of the measurement magnitudes). As for $\mathcal{R}(\theta)$, there are numerous options for regularization that may be chosen based on the problem physics which will be discussed in much detail in the following section.

To solve the inverse problem, many approaches are available including iterative (Tallman et al. 2017; Hallaji et al. 2014) or non-iterative methods, for example by applying factorization (Schmitt 2009; Gebauer and Hyvönen 2007), D-bar (Knudsen et al. 2009; Isaacson et al. 2006), or monotonicity (Garde and Staboulis 2017; Tamburrino et al. 2003; Tamburrino and Rubinacci 2002). In this article, we focus on iterative methods due to their effectiveness in facilitating increased resolution and application of problem constraints. In solving the problem of minimizing the functional in Eq. 4, we employ a Gauss-Newton regime equipped with a line-search to compute the step size s_k in the solution

$$\theta_k = \theta_{k-1} + s_k \bar{\theta} \tag{5}$$

where θ_k is the present estimate and $\bar{\theta}$ is the update at iteration k given by

$$\bar{\theta} = (J_\theta^T W^{-1} J_\theta + \Gamma_{\mathcal{R}}^{-1})^{-1} (J_\theta^T W^{-1} (d - U(\theta_{k-1})) \tag{6}$$

where $\Gamma_{\mathcal{R}}^{-1} = L_{\mathcal{R}}^T L_{\mathcal{R}}$ is the inverted prior covariance matrix related to the Cholesky factor/appropriate regularization matrix $L_{\mathcal{R}}$. Moreover, $J_\theta = \frac{\partial U(\theta)}{\partial \theta}$ is the Jacobian matrix. Regularization and computation of the Jacobian matrix will be further detailed in later sections.

Two-state problems

In a two-state problem, we aim to utilize two data sets, d_1 and d_2, to simultaneously image two structural states using a stacking method. These states could be, and are commonly, undamaged and damaged states with corresponding measurements d_1 and d_2, respectively. Correspondingly, we aim to estimate the distributions θ_1 and θ_2. To do this, we begin by designating the change in parameters between measurements d_1 and d_2 as $\Delta\theta$ resulting in

$$\theta_2 = \theta_1 + \Delta\theta \tag{7}$$

which may then be used in generating the two-state observation model*

$$\begin{aligned} d_1 &= U(\theta_1) + e_1 \\ d_2 &= U(\theta_1 + \Delta\theta) + e_2 \end{aligned} \tag{8}$$

where e_1 and e_2 are the measurement noises for measurements d_1 and d_2, respectively. We may then concatenate to obtain the following matrix representation

$$\underbrace{\begin{bmatrix} d_1 \\ d_2 \end{bmatrix}}_{\mathcal{D}} = \underbrace{\begin{bmatrix} U(\theta_1) \\ U(\theta_1 + \Delta\theta) \end{bmatrix}}_{U(\Theta)} + \underbrace{\begin{bmatrix} e_1 \\ e_2 \end{bmatrix}}_{\mathcal{E}} \tag{9}$$

where

$$\Theta = \begin{bmatrix} \theta_1 \\ \Delta\theta \end{bmatrix} \tag{10}$$

which can be conveniently used to write the stacked observation model

*This model has previously been referred to as *nonlinear difference imaging* (Smyl et al. 2018d; Liu et al. 2016, 2015a)

$$\mathcal{D} = U(\Theta) + \mathcal{E}. \tag{11}$$

Following Eq. 11, we may write the two-state functional to be minimized as

$$\Psi_2 = ||L_{\mathcal{E}}(\mathcal{D} - U(\Theta))||^2 + \mathcal{R}(\Theta) \tag{12}$$

where $\mathcal{R}(\Theta)$ is now a compound regularization functional which may incorporate prior information related to the physics of each structural state and $L_{\mathcal{E}}$ is the Cholesky factor defined as $L_{\mathcal{E}}^T L_{\mathcal{E}} = W_{\mathcal{E}}^{-1}$, where $W_{\mathcal{E}}$ is a block form of the stationary noise matrices for each state (W_{e_1} and W_{e_2}):

$$W_{\mathcal{E}} = \begin{bmatrix} W_{e_1} & \mathbf{0} \\ \mathbf{0} & W_{e_2} \end{bmatrix}. \tag{13}$$

In solving the minimization problem posed in Eq. 12, we again employ a Gauss-Newton approach by recasting Eq. 5 for the stacked parameterization as

$$\Theta_k = \Theta_{k-1} + s_k \bar{\Theta} \tag{14}$$

where $\bar{\Theta}$ is explicitly given by

$$\bar{\Theta} = (J_\Theta^T W_{\mathcal{E}}^{-1} J_\Theta + \Gamma_{\mathcal{R}}^{-1})^{-1} (J_\Theta^T W_{\mathcal{E}}^{-1} (\mathcal{D} - U(\Theta_{k-1})) \tag{15}$$

where the Jacobian $J_\Theta = \frac{\partial U}{\partial \Theta} \neq J_\theta$ and is given by

$$J_\Theta = \begin{bmatrix} \frac{\partial U(\theta_1)}{\partial \theta_1} & \mathbf{0} \\ \frac{\partial U(\theta_1+\Delta\theta)}{\partial(\theta_1+\Delta\theta)} & \frac{\partial U(\theta_1+\Delta\theta)}{\partial(\theta_1+\Delta\theta)} \end{bmatrix}. \tag{16}$$

Joint problems

Joint inverse problems aim to estimate different physical properties by simultaneously solving different tomographic problems. Often, the aim is to improve an individual modality's resolution and/or quantitative information by taking advantage of a complimentary modality's strength; for example, ERT is excellent at detecting sharp features whereas QSEI often offers smoother reconstructions. Therefore, when sharper features are desired in QSEI, joint imaging with ERT is advantageous. There are numerous approaches for solving such problems (Ward et al. 2014; Ehrhardt et al. 2014), most often used in medical or geophysical applications. In SHM, however, the use of joint inversion is scarce due to a general lack of available algorithms – an issue we aim to address herein.

In this work, we consider two kinds of joint problems (i) stacked joint models and (ii) stacked joint models with a common structural operator. The aim in (i) is simply to solve two stationary tomographic problems simultaneously and the aim in (ii) is to simultaneously reconstruct two stationary tomographic problems assuming the models have an underlying similarity in their structure (Haber and Oldenburg 1997). In essence, (ii) is an extension of (i); we will therefore first derive a joint imaging regime for (i).

Stacked joint models: We begin with the realization that there are two data sets, d_1 and d_2, corresponding to parameters ϑ_1 for imaging modality 1 and ϑ_2 corresponding to imaging modality 2, respectively. We reinforce that modalities 1 and 2 may relate to stationary problems with *entirely different physics*. The observation model is then

$$\begin{aligned} d_1 &= U_1(\vartheta_1) + e_1 \\ d_2 &= U_2(\vartheta_2) + e_2 \end{aligned} \tag{17}$$

which is similar to the observation model in non-linear difference imaging (Smyl et al. 2018d; Liu et al. 2016, 2015a). We note, however, that ϑ_1 and ϑ_2 are not fundamentally linked by any parameter related to a change of state and there are differences in the forward models for each problem, therefore we denote U_1 and U_2 separately. Moreover, since we are dealing with separate imaging modalities, e_1 and e_2 are not considered to be stationary and modeled separately (i.e., $W_{e_1} \neq W_{e_2}$). As in the previous subsection, we may conveniently concatenate as follows

$$\underbrace{\begin{bmatrix} d_1 \\ d_2 \end{bmatrix}}_{\mathcal{D}_\mathcal{J}} = \underbrace{\begin{bmatrix} U_1(\vartheta_1) \\ U_2(\vartheta_2) \end{bmatrix}}_{U_\mathcal{J}(\Theta_\mathcal{J})} + \underbrace{\begin{bmatrix} e_1 \\ e_2 \end{bmatrix}}_{\mathcal{E}_\mathcal{J}} \tag{18}$$

where the subscript $\mathcal{J}$ denotes "joint" and

$$\Theta_{\mathcal{J}} = \begin{bmatrix} \vartheta_1 \\ \vartheta_2 \end{bmatrix}. \tag{19}$$

We then formally write the stacked observation model

$$\mathcal{D}_{\mathcal{J}} = U_{\mathcal{J}}(\Theta_{\mathcal{J}}) + \mathcal{E}_{\mathcal{J}}. \tag{20}$$

Resulting from Eq. 20, we obtain the joint functional to minimize

$$\Psi_{\mathcal{J}} = ||L_{\mathcal{J}}(\mathcal{D}_{\mathcal{J}} - U_{\mathcal{J}}(\Theta_{\mathcal{J}}))||^2 + \mathcal{R}_{\mathcal{J}}(\Theta_{\mathcal{J}}) \tag{21}$$

where $L_{\mathcal{J}}$ is obtained using non-stationary noise statistics with Eq. 13 and $\mathcal{R}_{\mathcal{J}}(\Theta_{\mathcal{J}})$ is a compound regularization functional incorporating prior information related to the problem physics. Since the estimation parameters ϑ_1 and ϑ_2 are not fundamentally linked by a change of state and are treated independently, we require a different approach to solve the minimization problem than was used in previous subsection. Using the Gauss-Newton approach with

$$\Theta_{\mathcal{J}k} = \Theta_{\mathcal{J}k-1} + s_k \bar{\Theta}_{\mathcal{J}} \tag{22}$$

we stack the independent parameters from each modality using

$$\bar{\Theta}_{\mathcal{J}} = \begin{bmatrix} ({J_{\vartheta_1}}^T {W_{e_1}}^{-1} J_{\vartheta_1} + \Gamma_{\mathcal{R}}^{-1})^{-1} ({J_{\vartheta_1}}^T {W_{e_1}}^{-1} (d_1 - U_1(\vartheta_{1k-1})) \\ ({J_{\vartheta_2}}^T {W_{e_2}}^{-1} J_{\vartheta_2} + \Gamma_{\mathcal{R}}^{-1})^{-1} ({J_{\vartheta_2}}^T {W_{e_2}}^{-1} (d_2 - U_2(\vartheta_{2k-1})) \end{bmatrix}. \tag{23}$$

where $J_{\vartheta_1} = \frac{\partial U_1(\vartheta_1)}{\partial \vartheta_1}$ and $J_{\vartheta_2} = \frac{\partial U_2(\vartheta_2)}{\partial \vartheta_2}$.

Stacked joint models with a common structural operator: We again aim to jointly reconstruct parameters $[\vartheta_1, \vartheta_2]^T$ from data $[d_1, d_2]^T$. In this section, we assume that parameters ϑ_1 and ϑ_2 have a similar structure; for example, in the case of localized cracking in a structural member we may surmise that the localized changes in ϑ_1 and ϑ_2 are common in structure/geometry. To accomplish this, we require a common structural operator $\mathfrak{C}$, herein referred to as simply "structural operator." In this work, $\mathfrak{C}$ is defined as a term added to a cost functional which relates similarities in the spatial distributions of ϑ_1 and ϑ_2. There are many choices (Haber and Oldenburg 1997); here, we consider a simple thresholding operator accepting a normalized parameter $0 \leq \vartheta_n \leq 1$:

$$\mathfrak{C}(\vartheta_n) = \begin{cases} 1, & \text{if } \vartheta_n < \mathfrak{t}. \\ 0, & \text{otherwise.} \end{cases} \tag{24}$$

where $0 < \mathfrak{t} < 1$ is a threshold parameter and ϑ_n is obtained simply by normalizing with respect to the maximum value, i.e. $\vartheta_n = \frac{\vartheta}{\vartheta_{\max}}$. In the case that damage significantly decreases the parameters, i.e. $\vartheta_1 \to 0$ and $\vartheta_2 \to 0$ (and $\vartheta_n \to 0$ by default), Eq. 24 may be interpreted as an operator linking the spatial similarities in damage locations for low values of $\mathfrak{t}$.

To incorporate the structural operator $\mathfrak{C}$ into the inverse regime, we penalize the misfit by adding a structural cost functional

$$\Psi_{\mathfrak{C}} = \sum_{i=1}^{N} \mathfrak{C}\Big(\frac{\vartheta_{1,i}}{\vartheta_{1,\max}}\Big) - \mathfrak{C}\Big(\frac{\vartheta_{2,i}}{\vartheta_{2,\max}}\Big) \tag{25}$$

to the joint imaging functional (Eq. 21), thereby penalizing discrepancies between the solutions of ϑ_1 and ϑ_2 with N degrees of freedom as follows

$$\Psi_{\mathcal{J},\mathfrak{C}} = ||L_{\mathcal{J}}(\mathcal{D}_{\mathcal{J}} - U_{\mathcal{J}}(\Theta_{\mathcal{J}}))||^2 + \mathcal{R}_{\mathcal{J}}(\Theta_{\mathcal{J}}) + \kappa \Psi_{\mathfrak{C}} \tag{26}$$

where the scalar κ controls the weighting of the structural operator. In solving this problem, we may adopt the same regime provided in Eq. 23 with the updated objective functional in Eq 26.

Regularization and constrained optimization

In this section, we provide practical information that is useful in providing accurate prior information and constraints for stationary inverse problems, as they apply to imaging damage in structures. We begin with regularization techniques, which are essential for handling the ill-posedness of the inverse problems and incorporating spatial information related to the problem physics. Following, we discuss the numerical implementation of constraints to ensure solutions are physically realistic and to help improve the minimization behavior of the regimes. Lastly, a summary table and brief discussion of the derived frameworks will be provided.

Regularization

Standard least-squares methods generally fail at solving ill-posed problems – for this reason, we require regularization. We may also use regularization as a way of incorporating prior information in our minimization regimes, which is immensely helpful when the form of regularization closely matches the problem physics. As an example, it is well known that many forms of cracking have sharp features. Therefore, edge-preserving regularization (such as total variation (TV)) is well-suited for such a case. On the other hand, when a damage process is smoothly distributed, Tikhonov or weighted-smoothness regularization may be better choices (Smyl et al. 2018d). Since we are often interested in reconstructing damage which may smooth or sharp, we will detail all aforementioned regularization schemes which may be incorporated in the single-state, two-state, or joint imaging frameworks (recall that $\mathcal{R}$ denoted a regularization functional and $\Gamma_{\mathcal{R}}$ was a prior covariance matrix).

Tikhonov regularization Possibly the most simplistic regularization technique is Tikhonov regularization. In Tikhonov regularization, we consider the following functional with the subscript "T" denoting "Tikhonov"

$$\mathcal{R}_T = ||\Gamma_T \theta||^2 \tag{27}$$

where θ again represents the estimation parameter and Γ_T is given by

$$\Gamma_T = \alpha_T I \tag{28}$$

where I is the identity matrix and α_T is a weighting parameter. Of practical importance, α_T largely controls the smoothness of solutions and may be easily optimized using L-curve analysis (see (Mueller and Siltanen 2012) for details). While simple, Tikhonov regularization is robust, easy to implement, and an efficient means to preliminary test a developed inverse algorithm.

Weighted-smoothness regularization Another regularization approach that is useful in cases where distributed parameters are expected to be smooth is weighted-smoothness regularization. In this technique, we use the regularization functional, with the subscript WS, given by

$$\mathcal{R}_{WS} = ||L_{WS}(\theta - \theta_{\text{exp}})||^2 \tag{29}$$

where θ_{exp} is obtained by determining the best homogeneous (one-parameter) estimate for θ and L_{WS} is the the Cholesky factorization of the matrix Γ_{WS}, (i.e. $\Gamma_{WS}^{-1} = {L_{WS}}^T L_{WS}$). Further, there are a multitude of ways to obtain θ_{exp}, however one simple method is to simply sweep an expected space of a homogeneous θ and find the minimum: $\theta_{\text{exp}} = \min||d - U(\theta_{\text{exp}})||$. Γ_{WS}, on the other hand, is determined element wise, where the matrix element (i, j) for a distributed parameter θ at locations x_i and x_j is given by

$$\Gamma_{WS}(i,j) = a \exp\Big(-\frac{||x_i - x_j||}{2b}\Big) + c\delta_{ij} \tag{30}$$

where the scalars a, b, and c are positive and δ_{ij} is the Kronecker delta function. In a basic sense, parameter a controls the weighting, b is incorporates spatial correlation, and c is small positive parameter which is used to guarantee that inverse of Γ_{WS} exists (Kaipio and Somersalo 2005). Therefore, this method offers more ability to be tuned to application-specific parameters than Tikhonov regularization; for example, one can directly control the smoothness of expected fluctuations in θ by adjusting b and also the regularization weighting via a and c. Where as Tikhonov regularization only allows for adjusting α_T. However, users should be aware that poor selection of a, b, and c may result in substandard reconstructions.

In addition, the use of weighted smoothness requires the addition of a gradient term in the Gauss-Newton schemes since the model is differential, unlike Tikhonov regularization. The gradient, updated at each iteration k, is given by

$$g_{WS} = \theta_{k-1} - \theta_{\exp}\Gamma_{WS}^T \tag{31}$$

and is incorporated into, for example, the one-state solution regime as follows

$$\bar{\theta} = (J_\theta^T W^{-1} J_\theta + \Gamma_{WS}^{-1})^{-1}(J_\theta^T W^{-1}(d - U(\theta_{k-1})) - g_{WS}). \tag{32}$$

Extension to the two-state and joint imaging regimes are also done in the same straight-forward manner.

Total Variation regularization Often, we are interested in reconstructing images where the parameter distribution has sharp edges or is blocky. In structural applications, such distributions may result from cracking, fracture propagation, localized plasticity, etc. (Seppänen et al. 2014a). While smoothness-promoting regularization methods can certainly be used in such cases (Tallman and Hernandez 2017), improved accuracy of damage location and distribution can be gained by using sharpness-promoting regularization. For this purpose, Total Variation regularization is most commonly used. For a parameter distribution θ, the isotropic TV functional is given by

$$\mathcal{R}_{TV}(\theta) = \alpha_{TV} \sum_{h=1}^{N} \sqrt{||(\nabla\theta)|_{e_h}||^2 + \beta} \tag{33}$$

where α_{TV} is the TV weighting parameter, $\nabla\theta|_{e_h}$ is the gradient of θ evaluated at degree of freedom e_h, and β is the stabilization parameter (i.e. when $\beta = 0$, the functional may not be differentiable). For a detailed discussion of TV regularization, including anisotropic TV and statistical incorporation of TV, we refer the reader to (González et al. 2017; Lassas and Siltanen 2004). We remark that TV can be quite challenging to use, particularly when the parameters α_{TV} and β are poorly selected. Some choices for selecting these parameters are detailed in, e.g. (Niinimaki et al. 2016). From experience with structural applications, the use of a confidence-based selection of α_{TV} and β following (González et al. 2017), has proven robust. In this work we select α_{TV} using

$$\alpha_{TV} = -\frac{\ln(1 - \frac{p_\alpha}{100})}{\theta_{\exp}/d} \tag{34}$$

where p_α is the % confidence that θ lies between $(0, \theta_{\exp})$ and d is the width of the finite element. For β we use

$$\beta = \zeta\left(\frac{\theta_{\exp}}{d}\right)^2 \tag{35}$$

where ζ is a small number. For general purposes, the values of $p_\alpha = 90.0\%$ and $\zeta = 10^{-3}$ have proven robust and are recommended as a starting point.

To implement TV in the imaging regime, we again require Γ_{TV} (also denoted as the TV Hessian) and gradient vectors, Γ_{TV} and g_{TV}, respectively. For Γ_{TV}, we use

$$\Gamma_{TV} = \alpha_{TV} \frac{\partial^2 \mathcal{R}_{TV}(\theta_i)}{\partial\theta^2} \tag{36}$$

where θ_i refers to the i^{th} degree of freedom in θ. Moreover, we may compute the gradient using

$$g_{TV} = \alpha_{TV} \frac{\partial \mathcal{R}_{TV}(\theta_i)}{\partial\theta}. \tag{37}$$

It is important to note that there are numerous regimes to compute the derivatives. Some choices include using finite differencing following (Lefkimmiatis et al. 2012) or Gateaux derivatives following (Vogel and Oman 1996). As in the previous subsection, Γ_{TV} and g_{TV} may be incorporated into any regime provided herein. For example, the one-state solution:

$$\bar{\theta} = (J_\theta^T W^{-1} J_\theta + \Gamma_{TV}^{-1})^{-1}(J_\theta^T W^{-1}(d - U(\theta_{k-1})) - g_{TV}). \tag{38}$$

Constraints

The use of constrained optimization is useful (if not, essential) in structural imaging problems for the following reasons (i) solutions can be constrained to real numbers (i.e. $\theta > 0$) avoiding numerical problems with forward operators and ensuring solutions are realistic, (ii) solutions may be bounded between known physical limitations (say $0 < \theta < \theta_{\text{impossible}}$), and (iii) often, constraints result in faster minimization since the solution space is limited to a more feasible set. In the case of imaging structural damage, using for example ERT or QSEI, we can often place realistic constraints based on simple assumptions, such as the realization that damage can only decrease θ, resulting in ($0 < \theta \leq \theta_{\text{exp}}$) (Smyl et al. 2018d). Unfortunately, however, the practical implementation of constraints in structural imaging problems is rarely reported. In this subsection, we will address this by providing a simple method for constraining the imaging frameworks provided herein.

There are two components to constraining the regimes provided. First, we must penalize degrees of freedom that are near or outside our specific constraint(s) in the objective function. Secondly, we must incorporate the first- (gradient) and second-order (Hessian) terms in our least squares update. For simplicity, we will illustrate this by considering the single-state problem and only consider upper and lower constraints for simplicity.

We may begin by defining a simple type of constraints using barrier functions, which is essentially an interior-point method. Let's first assume we have the following constraints: $q_1 = 0 < \theta < q_2$, where q_2 has a positive value. In this approach, we have barrier functions $\mathfrak{B}_k(\theta_i)$ where the $i = 1, \ldots, N$ are the degrees of freedom and $k = 1, 2$. In generating the barrier functions, we employ second order convex polynomials in the representation $\mathfrak{B}_k(\theta_i) = \varpi_k(\theta_i)\mathfrak{b}_k(\theta_i)$ where $\varpi_k(\theta_i)$ is a function defining an interval where the polynomial $\mathfrak{b}_k(\theta_i) = a_1\theta_i^2 + b_1\theta_i + c_1$ with coefficients a_1, b_1 and c_1 is turned on.

A nice feature of applying constraints in this way is its flexibility. One may select different locations for q_1 and q_2 in a manner which accurately represents the problem physics. Numerically speaking, however there are a few considerations (i) suppose we want to add the polynomial constraint at q_3, we must define the interval ϖ using a small barrier length ι, resulting in the interval $[q_3 - \iota, q_3]$ and (ii) non-negativity constraints must be slightly above zero to avoid issues with forward models, for example using the interval $[10^{-7}, 10^{-4}]$. In practice, these numerical realities rarely affect results.

To implement barrier functions into the cost function, we simply add barrier functionals (depending on whether the user wants to add 1 or 2 barrier functions) using

$$\Psi_C = \kappa_C \sum_{i=1}^{N} \mathfrak{B}_k(\theta_i) \tag{39}$$

where κ_C is a positive constant that controls the weight of the constraint(s) and "C" denotes constraint. Lastly, we require the gradient and Hessian related to the constraints, which is done in a straight-forward manner by computing the vector of length N

$$g_C = \frac{d\mathfrak{B}_k(\theta_i)}{d\theta_i} \tag{40}$$

the square diagonal Hessian matrix (off diagonals are zeros) is computed by filling the diagonal with the following entries

$$\Gamma_C = \frac{d^2\mathfrak{B}_k(\theta_i)}{d\theta_i^2}. \tag{41}$$

As an example, we may incorporate the gradient and Hessian into the single-state regime as done previously:

$$\bar{\theta} = (J_\theta^T W^{-1} J_\theta + \Gamma_{\mathcal{R}}^{-1} + \Gamma_C)^{-1}(J_\theta^T W^{-1}(d - U(\theta_{k-1})) - g_C). \tag{42}$$

Mixed regularization with constraints

In previous problems, we considered functionals utilizing the same regularization functional for each state. In many cases, however, we would like to apply different prior models and constraints to accurately represent the physics of each state. For example, in (Smyl et al. 2018d) the authors utilized the two-state approach considering (i) an initial undamaged state where the parameters θ_1 were assumed to be smoothly distributed and (ii) the second state where the

cracking was assumed to result in sharp distributions of $\Delta\theta$. To accomplish this, the researchers utilized compound regularization in the form

$$\mathcal{R}(\theta) = \mathcal{R}_{WS}(\theta_1) + \mathcal{R}_{TV}(\Delta\theta). \tag{43}$$

Clearly, there are numerous combinations of mixed regularization that may be employed to accurately incorporate prior models relevant to states' physics – when using multiple data sets with stacking or joint inversion. Moreover, models such as Eq. 43 offer advantages over non-stacked models, since much of the noise and modeling errors may be absorbed in the (often) uninteresting distribution of θ_1 (Liu et al. 2016, 2015a).

Incorporation of mixed regularization in two-state least squares regimes may be done in many ways. In the case of the compound functional in Eq. 43, we may, for example write a mixed regularization block-diagonal matrix Γ_{MR} as follows

$$\Gamma_{MR} = \begin{bmatrix} \Gamma_{WS} & \mathbf{0} \\ \mathbf{0} & \Gamma_{TV} \end{bmatrix}. \tag{44}$$

or simply use mapping matrices for each state, as detailed in (Liu et al. 2015b). The choice is mostly dependent on the users' data structure. In the case of the prior model gradients, we may simply concatenate gradient vectors yielding g_{MR}, although mapping matrices may also be used. Compiling these realizations, again considering the compound functional in Eq. 43, we may write the compound regularization of the constrained two-state problem

$$\Psi_{2,MR} = ||L_{\mathcal{E}}(\mathcal{D} - U(\Theta))||^2 + \mathcal{R}_{WS}(\theta_1) + \mathcal{R}_{TV}(\Delta\theta) + \Psi_C \tag{45}$$

in general, however, we may write

$$\Psi_{2,MR} = ||L_{\mathcal{E}}(\mathcal{D} - U(\Theta))||^2 + \mathcal{R}_1(\theta_1) + \mathcal{R}_2(\Delta\theta) + \Psi_C \tag{46}$$

where the subscript "MR" denotes the use of mixed regularization functionals and $\mathcal{R}_1$ and $\mathcal{R}_2$ are the appropriate regularization functionals chosen by the user.

In the case of the joint regimes, we obtain a similar result for the functionals. For example, we may consider the functional for joint imaging with a structural operator and mixed regularization terms given by

$$\Psi_{\mathcal{J},\mathfrak{C}} = ||L_{\mathcal{J}}(\mathcal{D}_{\mathcal{J}} - U_{\mathcal{J}}(\Theta_{\mathcal{J}}))||^2 + \mathcal{R}_{\mathcal{J},1}(\vartheta_1) + \mathcal{R}_{\mathcal{J},2}(\vartheta_2) + \kappa\Psi_{\mathfrak{C}} \tag{47}$$

where $\mathcal{R}_{\mathcal{J},1}$ and $\mathcal{R}_{\mathcal{J},2}$ are simply the selected regularization functional for the appropriate physics representing parameters ϑ_1 and ϑ_2, respectively. To obtain the least-squares update for the joint approaches, we may simply modify Eq. 23 with the appropriate regularization matrix and gradient vector.

Framework summary

At this point, the reader may notice that constraint Hessians, constraint gradients, prior covariance matrices, and regularization gradients are simply added or subtracted to the least squares updates. Moreover, the reader may also note that the integration of constraints and different regularization techniques to the cost function may be done by just selecting, adding, and/or removing the desired functionals. This flexibility is one primary advantage of the proposed frameworks, although it may add some ambiguity to new users. For this purpose, Table 1 is provided to summarize all cost functionals and least-squares updates for the 38 frameworks provided in this work (representing all combinations of regularization methods, constraints, and models).

Remark: As a health warning, the use of unregularized approaches is, in general, not recommended due to the ill-posed nature of many inverse problems in SHM. In some special cases of tomography, however, the use of regularization is not necessarily required, potentially owing to a low condition number (a metric for how ill-conditioned a problem is) (Aster et al. 2018). Some cases may include DIC applications employing optical flow (Smyl et al. 2018a) or some applications of radiation-based tomography with low noise and numerous measurements (Chen et al. 2016). For completeness, we have included the unregularized frameworks in Table 1. Moreover, constraints should be used wisely; for example in single-state problems where complex numbers are not expected, the constraint $\theta \geq 0$ is both simple to employ and very useful.

Tomographic frameworks

		Single-state	Two-state	Joint - stacked	Joint - structural operator
UC/UR	CF	$\Psi_1 = \|\|L_e(d - U(\theta))\|\|^2$	$\Psi_2 = \|\|L_\mathcal{E}(\mathcal{D} - U(\Theta))\|\|^2$	$\Psi_\mathcal{J} = \|\|L_\mathcal{J}(\mathcal{D}_\mathcal{J} - U_\mathcal{J}(\Theta_\mathcal{J}))\|\|^2$	$\Psi_{\mathcal{J},\mathcal{E}} = \|\|L_\mathcal{J}(\mathcal{D}_\mathcal{J} - U_\mathcal{J}(\Theta_\mathcal{J}))\|\|^2 + \kappa\Psi_\mathcal{E}$
	LS	$\bar{\theta} = (J_\theta^T W^{-1} J_\theta)^{-1}(J_\theta^T W^{-1}(d - U(\theta_{k-1}))$	$\bar{\Theta} = (J_\Theta^T W_\mathcal{E}^{-1} J_\Theta)^{-1}(J_\Theta^T W_\mathcal{E}^{-1}(\mathcal{D} - U(\Theta_{k-1}))$	$\bar{\Theta}_\mathcal{J} = \begin{bmatrix}(J_{\vartheta_1}{}^T W_{e_1}{}^{-1} J_{\vartheta_1})^{-1}(J_{\vartheta_1}{}^T W_{e_1}{}^{-1}(d_1 - U_1(\vartheta_{1k-1}))\\ (J_{\vartheta_2}{}^T W_{e_2}{}^{-1} J_{\vartheta_2})^{-1}(J_{\vartheta_2}{}^T W_{e_2}{}^{-1}(d_2 - U_2(\vartheta_{2k-1}))\end{bmatrix}$	$\bar{\Theta}_{\mathcal{J},\mathcal{E}} = \bar{\Theta}_\mathcal{J}$
UC/Tik	CF	$\Psi_1 = \|\|L_e(d - U(\theta))\|\|^2 + \mathcal{R}_T(\theta)$	$\Psi_2 = \|\|L_\mathcal{E}(\mathcal{D} - U(\Theta))\|\|^2 + \mathcal{R}_\mathcal{T}(\Theta)$	$\Psi_\mathcal{J} = \|\|L_\mathcal{J}(\mathcal{D}_\mathcal{J} - U_\mathcal{J}(\Theta_\mathcal{J}))\|\|^2 + \mathcal{R}_\mathcal{T}(\Theta_\mathcal{J})$	$\Psi_{\mathcal{J},\mathcal{E}} = \|\|L_\mathcal{J}(\mathcal{D}_\mathcal{J} - U_\mathcal{J}(\Theta_\mathcal{J}))\|\|^2 + \mathcal{R}_\mathcal{T}(\Theta_\mathcal{J}) + \kappa\Psi_\mathcal{E}$
	LS	$\bar{\theta} = (J_\theta^T W^{-1} J_\theta + \Gamma_T^{-1})^{-1}(J_\theta^T W^{-1}(d - U(\theta_{k-1}))$	$\bar{\Theta} = (J_\Theta^T W_\mathcal{E}^{-1} J_\Theta + \Gamma_T^{-1})^{-1}(J_\Theta^T W_\mathcal{E}^{-1}(\mathcal{D} - U(\Theta_{k-1}))$	$\bar{\Theta}_\mathcal{J} = \begin{bmatrix}(J_{\vartheta_1}{}^T W_{e_1}{}^{-1} J_{\vartheta_1} + \Gamma_T^{-1})^{-1}(J_{\vartheta_1}{}^T W_{e_1}{}^{-1}(d_1 - U_1(\vartheta_{1k-1}))\\ (J_{\vartheta_2}{}^T W_{e_2}{}^{-1} J_{\vartheta_2} + \Gamma_T^{-1})^{-1}(J_{\vartheta_2}{}^T W_{e_2}{}^{-1}(d_2 - U_2(\vartheta_{2k-1}))\end{bmatrix}$	$\bar{\Theta}_{\mathcal{J},\mathcal{E}} = \bar{\Theta}_\mathcal{J}$
UC/WS	CF	$\Psi_1 = \|\|L_e(d - U(\theta))\|\|^2 + \mathcal{R}_{WS}(\theta)$	$\Psi_2 = \|\|L_\mathcal{E}(\mathcal{D} - U(\Theta))\|\|^2 + \mathcal{R}_{WS}(\Theta)$	$\Psi_\mathcal{J} = \|\|L_\mathcal{J}(\mathcal{D}_\mathcal{J} - U_\mathcal{J}(\Theta_\mathcal{J}))\|\|^2 + \mathcal{R}_{WS}(\Theta_\mathcal{J})$	$\Psi_{\mathcal{J},\mathcal{E}} = \|\|L_\mathcal{J}(\mathcal{D}_\mathcal{J} - U_\mathcal{J}(\Theta_\mathcal{J}))\|\|^2 + \mathcal{R}_{WS}(\Theta_\mathcal{J}) + \kappa\Psi_\mathcal{E}$
	LS	$\bar{\theta} = (J_\theta^T W^{-1} J_\theta + \Gamma_{WS}^{-1})^{-1}(J_\theta^T W^{-1}(d - U(\theta_{k-1})) - g_{WS})$	$\bar{\Theta} = (J_\Theta^T W_\mathcal{E}^{-1} J_\Theta + \Gamma_{WS}^{-1})^{-1}(J_\Theta^T W_\mathcal{E}^{-1}(\mathcal{D} - U(\Theta_{k-1})) - g_{WS})$	$\bar{\Theta}_\mathcal{J} = \begin{bmatrix}(J_{\vartheta_1}{}^T W_{e_1}{}^{-1} J_{\vartheta_1} + \Gamma_{WS}^{-1})^{-1}(J_{\vartheta_1}{}^T W_{e_1}{}^{-1}(d_1 - U_1(\vartheta_{1k-1})) - g_{WS})\\ (J_{\vartheta_2}{}^T W_{e_2}{}^{-1} J_{\vartheta_2} + \Gamma_{WS}^{-1})^{-1}(J_{\vartheta_2}{}^T W_{e_2}{}^{-1}(d_2 - U_2(\vartheta_{2k-1})) - g_{WS})\end{bmatrix}$	$\bar{\Theta}_{\mathcal{J},\mathcal{E}} = \bar{\Theta}_\mathcal{J}$
UC/TV	CF	$\Psi_1 = \|\|L_e(d - U(\theta))\|\|^2 + \mathcal{R}_{TV}(\theta)$	$\Psi_2 = \|\|L_\mathcal{E}(\mathcal{D} - U(\Theta))\|\|^2 + \mathcal{R}_{TV}(\Theta)$	$\Psi_\mathcal{J} = \|\|L_\mathcal{J}(\mathcal{D}_\mathcal{J} - U_\mathcal{J}(\Theta_\mathcal{J}))\|\|^2 + \mathcal{R}_{TV}(\Theta_\mathcal{J})$	$\Psi_{\mathcal{J},\mathcal{E}} = \|\|L_\mathcal{J}(\mathcal{D}_\mathcal{J} - U_\mathcal{J}(\Theta_\mathcal{J}))\|\|^2 + \mathcal{R}_{TV}(\Theta_\mathcal{J}) + \kappa\Psi_\mathcal{E}$
	LS	$\bar{\theta} = (J_\theta^T W^{-1} J_\theta + \Gamma_{TV}^{-1})^{-1}(J_\theta^T W^{-1}(d - U(\theta_{k-1})) - g_{TV})$	$\bar{\Theta} = (J_\Theta^T W_\mathcal{E}^{-1} J_\Theta + \Gamma_{WS}^{-1})^{-1}(J_\Theta^T W_\mathcal{E}^{-1}(\mathcal{D} - U(\Theta_{k-1})) - g_{TV})$	$\bar{\Theta}_\mathcal{J} = \begin{bmatrix}(J_{\vartheta_1}{}^T W_{e_1}{}^{-1} J_{\vartheta_1} + \Gamma_{TV}^{-1})^{-1}(J_{\vartheta_1}{}^T W_{e_1}{}^{-1}(d_1 - U_1(\vartheta_{1k-1})) - g_{TV})\\ (J_{\vartheta_2}{}^T W_{e_2}{}^{-1} J_{\vartheta_2} + \Gamma_{TV}^{-1})^{-1}(J_{\vartheta_2}{}^T W_{e_2}{}^{-1}(d_2 - U_2(\vartheta_{2k-1})) - g_{TV})\end{bmatrix}$	$\bar{\Theta}_{\mathcal{J},\mathcal{E}} = \bar{\Theta}_\mathcal{J}$
UC/MR	CF	*Not applicable*	$\Psi_2 = \|\|L_\mathcal{E}(\mathcal{D} - U(\Theta))\|\|^2 + \mathcal{R}_1(\theta_1) + \mathcal{R}_2(\Delta\theta)$	$\Psi_\mathcal{J} = \|\|L_\mathcal{J}(\mathcal{D}_\mathcal{J} - U_\mathcal{J}(\Theta_\mathcal{J}))\|\|^2 + \mathcal{R}_1(\vartheta_1) + \mathcal{R}_2(\vartheta_2)$	$\Psi_{\mathcal{J},\mathcal{E}} = \|\|L_\mathcal{J}(\mathcal{D}_\mathcal{J} - U_\mathcal{J}(\Theta_\mathcal{J}))\|\|^2 + \mathcal{R}_1(\vartheta_1) + \mathcal{R}_2(\vartheta_2) + \kappa\Psi_\mathcal{E}$
	LS	*Not applicable*	$\bar{\Theta} = (J_\Theta^T W_\mathcal{E}^{-1} J_\Theta + \Gamma_{MR}^{-1})^{-1}(J_\Theta^T W_\mathcal{E}^{-1}(\mathcal{D} - U(\Theta_{k-1})) - g_{MR})$	$\bar{\Theta}_\mathcal{J} = \begin{bmatrix}(J_{\vartheta_1}{}^T W_{e_1}{}^{-1} J_{\vartheta_1} + \Gamma_{MR}^{-1})^{-1}(J_{\vartheta_1}{}^T W_{e_1}{}^{-1}(d_1 - U_1(\vartheta_{1k-1})) - g_{MR})\\ (J_{\vartheta_2}{}^T W_{e_2}{}^{-1} J_{\vartheta_2} + \Gamma_{MR}^{-1})^{-1}(J_{\vartheta_2}{}^T W_{e_2}{}^{-1}(d_2 - U_2(\vartheta_{2k-1})) - g_{MR})\end{bmatrix}$	$\bar{\Theta}_{\mathcal{J},\mathcal{E}} = \bar{\Theta}_\mathcal{J}$
C/UR	CF	$\Psi_1 = \|\|L_e(d - U(\theta))\|\|^2 + \kappa_C\Psi_C$	$\Psi_2 = \|\|L_\mathcal{E}(\mathcal{D} - U(\Theta))\|\|^2 + \kappa_C\Psi_C$	$\Psi_\mathcal{J} = \|\|L_\mathcal{J}(\mathcal{D}_\mathcal{J} - U_\mathcal{J}(\Theta_\mathcal{J}))\|\|^2 + \kappa_C\Psi_C$	$\Psi_{\mathcal{J},\mathcal{E}} = \|\|L_\mathcal{J}(\mathcal{D}_\mathcal{J} - U_\mathcal{J}(\Theta_\mathcal{J}))\|\|^2 + \kappa\Psi_\mathcal{E} + \kappa_C\Psi_C$
	LS	$\bar{\theta} = (J_\theta^T W^{-1} J_\theta + \Gamma_C)^{-1}(J_\theta^T W^{-1}(d - U(\theta_{k-1})) - g_C)$	$\bar{\Theta} = (J_\Theta^T W_\mathcal{E}^{-1} J_\Theta + \Gamma_C)^{-1}(J_\Theta^T W_\mathcal{E}^{-1}(\mathcal{D} - U(\Theta_{k-1})) - g_C)$	$\bar{\Theta}_\mathcal{J} = \begin{bmatrix}(J_{\vartheta_1}{}^T W_{e_1}{}^{-1} J_{\vartheta_1} + \Gamma_C)^{-1}(J_{\vartheta_1}{}^T W_{e_1}{}^{-1}(d_1 - U_1(\vartheta_{1k-1})) - g_C)\\ (J_{\vartheta_2}{}^T W_{e_2}{}^{-1} J_{\vartheta_2} + \Gamma_C)^{-1}(J_{\vartheta_2}{}^T W_{e_2}{}^{-1}(d_2 - U_2(\vartheta_{2k-1})) - g_C)\end{bmatrix}$	$\bar{\Theta}_{\mathcal{J},\mathcal{E}} = \bar{\Theta}_\mathcal{J}$
C/Tik	CF	$\Psi_1 = \|\|L_e(d - U(\theta))\|\|^2 + \mathcal{R}_T(\theta) + \kappa_C\Psi_C$	$\Psi_2 = \|\|L_\mathcal{E}(\mathcal{D} - U(\Theta))\|\|^2 + \mathcal{R}_T(\Theta) + \kappa_C\Psi_C$	$\Psi_\mathcal{J} = \|\|L_\mathcal{J}(\mathcal{D}_\mathcal{J} - U_\mathcal{J}(\Theta_\mathcal{J}))\|\|^2 + \mathcal{R}_T(\Theta_\mathcal{J}) + \kappa_C\Psi_C$	$\Psi_{\mathcal{J},\mathcal{E}} = \|\|L_\mathcal{J}(\mathcal{D}_\mathcal{J} - U_\mathcal{J}(\Theta_\mathcal{J}))\|\|^2 + \mathcal{R}_T(\Theta_\mathcal{J}) + \kappa\Psi_\mathcal{E} + \kappa_C\Psi_C$
	LS	$\bar{\theta} = (J_\theta^T W^{-1} J_\theta + \Gamma_T^{-1} + \Gamma_C)^{-1}(J_\theta^T W^{-1}(d - U(\theta_{k-1})) - g_C)$	$\bar{\Theta} = (J_\Theta^T W_\mathcal{E}^{-1} J_\Theta + \Gamma_T^{-1} + \Gamma_C)^{-1}(J_\Theta^T W_\mathcal{E}^{-1}(\mathcal{D} - U(\Theta_{k-1})) - g_C)$	$\bar{\Theta}_\mathcal{J} = \begin{bmatrix}(J_{\vartheta_1}{}^T W_{e_1}{}^{-1} J_{\vartheta_1} + \Gamma_T^{-1} + \Gamma_C)^{-1}(J_{\vartheta_1}{}^T W_{e_1}{}^{-1}(d_1 - U_1(\vartheta_{1k-1})) - g_C)\\ (J_{\vartheta_2}{}^T W_{e_2}{}^{-1} J_{\vartheta_2} + \Gamma_T^{-1} + \Gamma_C)^{-1}(J_{\vartheta_2}{}^T W_{e_2}{}^{-1}(d_2 - U_2(\vartheta_{2k-1})) - g_C)\end{bmatrix}$	$\bar{\Theta}_{\mathcal{J},\mathcal{E}} = \bar{\Theta}_\mathcal{J}$
C/WS	CF	$\Psi_1 = \|\|L_e(d - U(\theta))\|\|^2 + \mathcal{R}_{WS}(\theta) + \kappa_C\Psi_C$	$\Psi_2 = \|\|L_\mathcal{E}(\mathcal{D} - U(\Theta))\|\|^2 + \mathcal{R}_{WS}(\Theta) + \kappa_C\Psi_C$	$\Psi_\mathcal{J} = \|\|L_\mathcal{J}(\mathcal{D}_\mathcal{J} - U_\mathcal{J}(\Theta_\mathcal{J}))\|\|^2 + \mathcal{R}_{WS}(\Theta_\mathcal{J}) + \kappa_C\Psi_C$	$\Psi_{\mathcal{J},\mathcal{E}} = \|\|L_\mathcal{J}(\mathcal{D}_\mathcal{J} - U_\mathcal{J}(\Theta_\mathcal{J}))\|\|^2 + \mathcal{R}_{WS}(\Theta_\mathcal{J}) + \kappa\Psi_\mathcal{E} + \kappa_C\Psi_C$
	LS	$\bar{\theta} = (J_\theta^T W^{-1} J_\theta + \Gamma_{WS}^{-1} + \Gamma_C)^{-1}(J_\theta^T W^{-1}(d - U(\theta_{k-1})) - g_{WS} - g_C)$	$\bar{\Theta} = (J_\Theta^T W_\mathcal{E}^{-1} J_\Theta + \Gamma_{WS}^{-1} + \Gamma_C)^{-1}(J_\Theta^T W_\mathcal{E}^{-1}(\mathcal{D} - U(\Theta_{k-1})) - g_{WS} - g_C)$	$\bar{\Theta}_\mathcal{J} = \begin{bmatrix}(J_{\vartheta_1}{}^T W_{e_1}{}^{-1} J_{\vartheta_1} + \Gamma_{WS}^{-1} + \Gamma_C)^{-1}(J_{\vartheta_1}{}^T W_{e_1}{}^{-1}(d_1 - U_1(\vartheta_{1k-1})) - g_{WS} - g_C)\\ (J_{\vartheta_2}{}^T W_{e_2}{}^{-1} J_{\vartheta_2} + \Gamma_{WS}^{-1} + \Gamma_C)^{-1}(J_{\vartheta_2}{}^T W_{e_2}{}^{-1}(d_2 - U_2(\vartheta_{2k-1})) - g_{WS} - g_C)\end{bmatrix}$	$\bar{\Theta}_{\mathcal{J},\mathcal{E}} = \bar{\Theta}_\mathcal{J}$
C/TV	CF	$\Psi_1 = \|\|L_e(d - U(\theta))\|\|^2 + \mathcal{R}_{TV}(\theta) + \kappa_C\Psi_C$	$\Psi_2 = \|\|L_\mathcal{E}(\mathcal{D} - U(\Theta))\|\|^2 + \mathcal{R}_{TV}(\Theta) + \kappa_C\Psi_C$	$\Psi_\mathcal{J} = \|\|L_\mathcal{J}(\mathcal{D}_\mathcal{J} - U_\mathcal{J}(\Theta_\mathcal{J}))\|\|^2 + \mathcal{R}_{TV}(\Theta_\mathcal{J}) + \kappa_C\Psi_C$	$\Psi_{\mathcal{J},\mathcal{E}} = \|\|L_\mathcal{J}(\mathcal{D}_\mathcal{J} - U_\mathcal{J}(\Theta_\mathcal{J}))\|\|^2 + \mathcal{R}_{TV}(\Theta_\mathcal{J}) + \kappa\Psi_\mathcal{E} + \kappa_C\Psi_C$
	LS	$\bar{\theta} = (J_\theta^T W^{-1} J_\theta + \Gamma_{TV}^{-1} + \Gamma_C)^{-1}(J_\theta^T W^{-1}(d - U(\theta_{k-1})) - g_{TV} - g_C)$	$\bar{\Theta} = (J_\Theta^T W_\mathcal{E}^{-1} J_\Theta + \Gamma_{TV}^{-1} + \Gamma_C)^{-1}(J_\Theta^T W_\mathcal{E}^{-1}(\mathcal{D} - U(\Theta_{k-1})) - g_{TV} - g_C)$	$\bar{\Theta}_\mathcal{J} = \begin{bmatrix}(J_{\vartheta_1}{}^T W_{e_1}{}^{-1} J_{\vartheta_1} + \Gamma_{TV}^{-1} + \Gamma_C)^{-1}(J_{\vartheta_1}{}^T W_{e_1}{}^{-1}(d_1 - U_1(\vartheta_{1k-1})) - g_{TV} - g_C)\\ (J_{\vartheta_2}{}^T W_{e_2}{}^{-1} J_{\vartheta_2} + \Gamma_{TV}^{-1} + \Gamma_C)^{-1}(J_{\vartheta_2}{}^T W_{e_2}{}^{-1}(d_2 - U_2(\vartheta_{2k-1})) - g_{TV} - g_C)\end{bmatrix}$	$\bar{\Theta}_{\mathcal{J},\mathcal{E}} = \bar{\Theta}_\mathcal{J}$
C/MR	CF	*Not applicable*	$\Psi_2 = \|\|L_\mathcal{E}(\mathcal{D} - U(\Theta))\|\|^2 + \mathcal{R}_1(\theta_1) + \mathcal{R}_2(\Delta\theta) + \kappa_C\Psi_C$	$\Psi_\mathcal{J} = \|\|L_\mathcal{J}(\mathcal{D}_\mathcal{J} - U_\mathcal{J}(\Theta_\mathcal{J}))\|\|^2 + \mathcal{R}_1(\vartheta_1) + \mathcal{R}_2(\vartheta_2) + \kappa_C\Psi_C$	$\Psi_{\mathcal{J},\mathcal{E}} = \|\|L_\mathcal{J}(\mathcal{D}_\mathcal{J} - U_\mathcal{J}(\Theta_\mathcal{J}))\|\|^2 + \mathcal{R}_1(\vartheta_1) + \mathcal{R}_2(\vartheta_2) + \kappa\Psi_\mathcal{E} + \kappa_C\Psi_C$
	LS	*Not applicable*	$\bar{\Theta} = (J_\Theta^T W_\mathcal{E}^{-1} J_\Theta + \Gamma_{MR}^{-1} + \Gamma_C)^{-1}(J_\Theta^T W_\mathcal{E}^{-1}(\mathcal{D} - U(\Theta_{k-1})) - g_{MR} - g_C)$	$\bar{\Theta}_\mathcal{J} = \begin{bmatrix}(J_{\vartheta_1}{}^T W_{e_1}{}^{-1} J_{\vartheta_1} + \Gamma_{MR}^{-1} + \Gamma_C)^{-1}(J_{\vartheta_1}{}^T W_{e_1}{}^{-1}(d_1 - U_1(\vartheta_{1k-1})) - g_{MR} - g_C)\\ (J_{\vartheta_2}{}^T W_{e_2}{}^{-1} J_{\vartheta_2} + \Gamma_{MR}^{-1} + \Gamma_C)^{-1}(J_{\vartheta_2}{}^T W_{e_2}{}^{-1}(d_2 - U_2(\vartheta_{2k-1})) - g_{MR} - g_C)\end{bmatrix}$	$\bar{\Theta}_{\mathcal{J},\mathcal{E}} = \bar{\Theta}_\mathcal{J}$

Table 1. Summary of tomographic frameworks provided in this work, including single-state, two-state, joint - stacked, and joint - structural operator approaches. For this, the cost function (CF) and least-squares updates (LS) are provided as indicated in the far left columns. For brevity, the shorthand abbreviations were used: unconstrained (UC), constrained (C), unregularized (UR), Tikhonov regularization (Tik), weighted-smoothness regularization (WS), Total Variation Regularization (TV), and mixed regularization (MR).

Applying the inverse frameworks to ERT, QSEI, and joint ERT/QSEI

This section aims to integrate some of the one-state, two-state, and joint approaches in practical applications using two promising SHM imaging modalities: ERT and QSEI. Since 38 modalities were provided (cf. Table 1), we select only a few of the frameworks for demonstration purposes. To accomplish this, we start by detailing the integration of ERT and QSEI in some of the frameworks provided. Following, we provide some examples using data generated from experiments and simulation. Lastly, we discuss the results.

ERT

In ERT, we aim to reconstruct the electrical conductivity σ from potential measurements V. For this, the dependence of σ on electrode potentials U is modeled by the Complete Electrode Model (CEM) which consists of the differential equation

$$\nabla \cdot (\sigma \nabla u) = 0, \quad x \in \Omega \tag{48}$$

and the boundary conditions

$$u + \xi_l \sigma \frac{du}{d\bar{n}} = U_l, \quad x \in e_\ell, \ \ell = 1, \ldots, L \tag{49}$$

$$\sigma \frac{du}{d\bar{n}} = 0, \quad x \in \partial\Omega \backslash \bigcup_{\ell=1}^{L} e_\ell \tag{50}$$

$$\int_{e_l} \sigma \frac{du}{d\bar{n}} \, dS = I_l, \quad \ell = 1, \ldots, L \tag{51}$$

where Ω is the domain, $\partial\Omega$ is its boundary, u is the electric potential, $\bar{n}$ is the unit normal, and e_l represents the l^{th} electrode (Cheng et al. 1989; Somersalo et al. 1992). Additionally, ξ_l, U_l and I_l are the contact impedance, electric potential, and electrical current corresponding to electrode e_l. In the CEM, the current is conserved, by writing

$$\sum_{l=1}^{L} I_l = 0 \tag{52}$$

and the potential reference level must be fixed as follows

$$\sum_{l=1}^{L} U_l = 0. \tag{53}$$

To solve the CEM (Eqs. 48 - 53) using finite element modeling (FEM), we discretize the σ by approximating it using a piecewise linear basis following (Vauhkonen et al. 1999, 2001). Utilizing the single state observation model in Eq. 3, we note that, in ERT, we have $d = V$, $\theta = \sigma$, and the forward model is given by the CEM, resulting in the single-state ERT observation model

$$V = U(\sigma) + e. \tag{54}$$

resulting in the following regularized and constrained ERT functional to be minimized

$$\Psi_{ERT,1} = ||L_e(V - U(\sigma))||^2 + \mathcal{R}(\sigma) + \Psi_C \tag{55}$$

where the subscript $ERT, 1$ denotes the type of imaging (ERT) and the number of states (1) with the regularization and constraint types to be defined later.

For the two-state model, we have the initial state $\theta_1 = \sigma_1$, the change in state $\Delta\theta = \Delta\sigma$, and the second state $\theta_2 = \sigma_2 = \sigma_1 + \Delta\sigma$. Based on this, we may write the observation model for measurements V_1 and V_2

$$\begin{aligned} V_1 &= U(\sigma_1) + e_1 \\ V_2 &= U(\sigma_1 + \Delta\sigma) + e_2 \end{aligned} \tag{56}$$

where we may concatenate the solution vector following Eq. 10 using

$$\Theta_{ERT} = \begin{bmatrix} \theta_1 \\ \Delta\theta \end{bmatrix} = \begin{bmatrix} \sigma_1 \\ \Delta\sigma \end{bmatrix} \tag{57}$$

and the data vector using $\mathcal{D} = [V_1, V_2]^T$. By substitution, we may reformulate the generic functional in Eq. 12 as

$$\Psi_{ERT,2} = ||L_{\mathcal{E}}(\mathcal{D} - U(\Theta_{ERT}))||^2 + \mathcal{R}(\Theta_{ERT}) + \Psi_C. \tag{58}$$

To solve the single- and two-state ERT problems in Eqs. 55 and 58, respectively, we employ the Gauss-Newton method with the ERT Jacobian J_σ computed following (Vilhunen et al. 2002). This is done by substituting the appropriate data (V and $\mathcal{D}$), parameters (σ and Θ_{ERT}, regularization terms, and constraints into the least-squares regimes. In other words, by substituting into the LS updates in provided Table 1 and carrying through the Gauss-Newton regimes detailed in Section .

QSEI

In QSEI, we aim to find the inhomogeneous elastic modulus E using displacement fields u_m, knowledge of the structural geometry, and the external forces. In structural applications, u_m may be obtained, for example, from Digital Image Correlation (DIC) (Kang et al. 2007). In solving the QSEI problem, we require the forward model, which is solved using a well-known elasticity FEM regime, given by

$$U_j = \sum_{i=1}^{N_n} K_{ji}^{-1} F_i \tag{59}$$

where N_n is the number of unknown displacements, K_{ji}^{-1} is the compliance matrix, and F_i a force vector (Surana and Reddy 2016).

By corroborating this information with the generic frameworks, we note that, for the single-state problem, we have $\theta = E$ and $d = u_m$. Using Eq. 3, we may then write the single-state observation model

$$u_m = U(E) + e. \tag{60}$$

which results in in the following regularized and constrained QSEI functional to be minimized

$$\Psi_{QSEI,1} = ||L_e(u_m - U(E))||^2 + \mathcal{R}(E) + \Psi_C \tag{61}$$

where the subscripts follow the description provided in the previous subsection and the regularization and constraints are yet to be defined.

For the two-state model, we again have the initial state $\theta_1 = E_1$, the change in state $\Delta\theta = \Delta E$, and the second state $\theta_2 = E_2 = E_1 + \Delta E$. Based on this, we then write the observation model for measurements u_1 and u_2

$$\begin{aligned} u_1 &= U(E_1) + e_1 \\ u_2 &= U(E_1 + \Delta E) + e_2 \end{aligned} \tag{62}$$

where we concatenate the solution vector using

$$\Theta_{QSEI} = \begin{bmatrix} \theta_1 \\ \Delta\theta \end{bmatrix} = \begin{bmatrix} E_1 \\ \Delta E \end{bmatrix} \tag{63}$$

and the data vector $\mathcal{D} = [u_1, u_2]^T$. By substitution, we may reformulate the generic functional in Eq. 12 using the same methodology from the previous subsection as

$$\Psi_{QSEI,2} = ||L_{\mathcal{E}}(\mathcal{D} - U(\Theta_{QSEI}))||^2 + \mathcal{R}(\Theta_{QSEI}) + \Psi_C. \tag{64}$$

Lastly, the solution to Eq. 64 is preformed in the same manner specified in the final paragraph of the previous subsection with the j^{th} column of J_E computed using central differencing as follows

$$J_{E,j} = \frac{U(E_{k-1} + \Delta^J) - U(E_{k-1} - \Delta^J)}{2\Delta^J} \tag{65}$$

where Δ^J is a pertubation computed as a function of the machine precision ϵ using $\Delta^J = \sqrt[3]{\frac{\epsilon}{2}}$ following (An et al. 2011). We note that the central-difference perturbation method requires $2N_{el}$ solves of the of the forward model, where N_{el} refers to the number of elements (degrees of freedom, when the inverse problem is solved element wise). To reduce the computational demand by half, at the cost of the precision of J_E, we may use forward differencing, where the j^{th} column of J_E is given by

$$J_{E,j} = \frac{U(E_{k-1} + \Delta^J) - U(E_{k-1})}{\Delta^J}. \tag{66}$$

In cases where additional accuracy is required and the shape functions of K are accessible, one may also use the Adjoint Method, as described in (Oberai et al. 2003) or the semi-analytical method described in (Vilhunen et al. 2002).

Joint ERT/QSEI imaging

With ERT and QSEI modalities fully described, we now aim to combine both modalities into a joint imaging regime. We begin by defining the observation by substituting the appropriate ERT and QSEI parameters into Eq. 17. To do this, we first denote the separate forward models for ERT and QSEI using $U_{ERT} = U_1$ (Eqs. 48 - 53) and $U_{QSEI} = U_2$ (Eq. 59). Following, we prescribe ($\vartheta_1 = \sigma$) and ($\vartheta_2 = E$) and write the joint ERT/QSEI observation model as

$$\begin{aligned} V &= U_{ERT}(\sigma) + e_1 \\ u_m &= U_{QSEI}(E) + e_2 \end{aligned}. \tag{67}$$

Using Eq. 67, we may then write the joint/stacked parameterization

$$\Theta_{\mathcal{J},E/Q} = \begin{bmatrix} \sigma \\ E \end{bmatrix}. \tag{68}$$

where the subscript "$\mathcal{J}, E/Q$" denotes the parameter represents joint a ERT/QSEI parameter. Further, we write stacked observation model

$$\mathcal{D}_{\mathcal{J}} = U_{\mathcal{J}}(\Theta_{\mathcal{J},E/Q}) + \mathcal{E}_{\mathcal{J}}. \tag{69}$$

and the constrained and regularized solution to the joint problem with a structural operator as

$$\Psi_{\mathcal{J},E/Q} = ||L_{\mathcal{J}}(\mathcal{D}_{\mathcal{J}} - U_{\mathcal{J}}(\Theta_{\mathcal{J},E/Q}))||^2 + \mathcal{R}_{\mathcal{J}}(\Theta_{\mathcal{J},E/Q}) + \kappa\Psi_{\mathfrak{C}}. \tag{70}$$

where the regularization and constraint functions will be defined in the application section. Lastly, for clarity, we provide the entire least-squares estimate for this imaging regime explicitly as follows

$$\bar{\Theta}_{\mathcal{J}} = \begin{bmatrix} ({J_\sigma}^T {W_{e_1}}^{-1} J_\sigma + \Gamma_{\mathcal{R}}^{-1} + \Gamma_C)^{-1} ({J_\sigma}^T {W_{e_1}}^{-1} (V - U_{ERT}(\sigma_{k-1})) - g_C) \\ ({J_E}^T {W_{e_2}}^{-1} J_E + \Gamma_{\mathcal{R}}^{-1} + \Gamma_C)^{-1} ({J_E}^T {W_{e_2}}^{-1} (u_m - U_{QSEI}(E_{k-1})) - g_C) \end{bmatrix} \tag{71}$$

where the appropriate regularization gradient should be applied to the right-hand sides when employing weighted smoothness or TV functionals.

Tomographic applications

This section provides examples of one-state, two-state, and joint tomographic imaging of structural members of various geometries. We begin by using experimental and simulated data to image cracking processes in reinforced concrete beams using ERT, both single-state and two-state imaging is applied. Following, simulated QSEI data is used to image damage in plates with single- and two-state approaches. Lastly, we use joint ERT/QSEI imaging for detecting damage in a simulated plate.

ERT imaging of cracked concrete beams

To demonstrate the efficacy of one- and two-state ERT, we utilize experimental data from (Smyl et al. 2018d). In the experiment, a 152 × 508 × 152 mm lightly-reinforced concrete beam was loaded in three-point bending. On the surface of the beam, a silver sensing skin with 28 copper boundary electrodes was applied for use in ERT measurements (cf. the left column of Fig.1). A total of 54 1.0 mA direct current injections were applied between electrodes i and j, $i = 6, 21$ and $j = 1, ..., 28, i \neq j$. Corresponding to each current injection, 1,458 adjacent electrode potentials were measured.

For the reconstructions, we utilized a rectangular FEM mesh with $N_{el} = 9{,}680$ triangular elements and $N_n = 5,047$ nodes. Since the problem was solve node-wise, this resulted in 5,047 degrees of freedom for each reconstructed state. In solving the problems, we selected three different regularization methods, including Tikhonov, WS, and TV denoted as $\mathcal{R}_\sigma = \mathcal{R}_T, \mathcal{R}_{WS}$, and $\mathcal{R}_{TV}$, respectively. For this, we chose the respective regularization parameters as $\lambda = 10^{-3}$, the weighted smoothness parameters $a = 10^{-2}$, $b = 0.5$, and $c = 10^{-3}$, and TV regularization with $p_\alpha = 90\%$ and $\zeta = 10^{-5}$. For the initial guess, we set $\sigma = \sigma_{\text{exp}}$, where σ_{exp} is the one-parameter homogeneous estimate. In addition, we apply a positivity constraint $\Psi_C^1 = \Psi_C^1(\sigma > 0)$ and an upper constraint $\Psi_C^2 = \Psi_C^2(\sigma < \sigma_{\text{ref}})$, where the superscript is simply an index for keeping track of the constraints and $\kappa_C = 10^{-3}$. We recall that Ψ_C^1 results from the fact that conductivity is always a positive value and Ψ_C^2 results from the assumption that cracking can only reduce σ with respect to the reference state. We then obtain the following minimization problem

$$\Psi_{ERT,1} = \arg \min_{\substack{\sigma>0 \\ \sigma<\sigma_{\text{ref}}}} \left[||L_e(V - U(\sigma))||^2 + \mathcal{R}_\sigma + \Psi_C^1(\sigma) + \Psi_C^2(\sigma)\right]. \tag{72}$$

For the two-state problem, we select different combinations of regularization functionals (denoted $\mathcal{R}_{\sigma_1}$ and $\mathcal{R}_{\Delta\sigma}$, respectively) for reconstructing σ_1 and $\Delta\sigma$. Since σ_1 is undamaged and assumed to be distributed smoothly, we choose Tikhonov and WS regularization in estimating σ_1. On the other hand, $\Delta\sigma$ is expected to have sharp changes due to cracking; therefore, both Tikhonov and TV regularization are chosen. For the initial guess in the two-state problem, we set $\Theta_{ERT} = [\sigma_{\text{exp}}, \mathbf{0}]$, where the initial guess for $\Delta\sigma = \mathbf{0}$ is a zero vector. For the constraints, we set $\Psi_C^3 = \Psi_C^3(\sigma_1 > 0)$, $\Psi_C^4 = \Psi_C^4(\sigma_2 \geq 0)$, and $\Psi_C^5 = \Psi_C^5(\Delta\sigma \leq 0)$ (since cracking can only reduce the conductivity of the sensing skin). Based on these realizations, we have the following two-state minimization problem

$$\Psi_{ERT,2} = \arg \min_{\substack{\sigma_1>0 \\ \sigma_2\geq 0 \\ \Delta\sigma\leq 0}} \left[||L_{\mathcal{E}}(\mathcal{D} - U(\Theta_{ERT}))||^2 + \mathcal{R}_{\sigma_1}(\sigma_1) + \mathcal{R}_{\Delta\sigma}(\Delta\sigma) + \Psi_C^3(\sigma_1) + \Psi_C^4(\sigma_2) + \Psi_C^5(\Delta\sigma)\right]. \tag{73}$$

Moreover, since we are interested in comparing both one- and two-state reconstructions of cracking, we normalize reconstructions of σ and σ_2 as detailed in (Smyl et al. 2018d). The normalized one- and two-state solutions are written as $\sigma_{n,1} = \frac{\sigma}{\sigma_{\text{ref}}}$ and $\sigma_{n,2} = \frac{\sigma_2}{\sigma_1}$, where each estimate ranges from 0 (cracked area) to 1 (background value). Reconstructions, showing unitless $\sigma_{n,1}$ and $\sigma_{n,2}$, for these cases are shown in Fig. 1.

Reconstructions in Fig. 1 clearly show that, with the exception of the one-state reconstruction using $\mathcal{R}_T$, the one- and two-state frameworks localized both cracks. Images in Fig. 1, therefore support the feasibility of the proposed frameworks for use in ERT imaging of discrete structural damage. It is important to remark that, while the two-state estimates generally capture both crack geometries better than the the one-state estimates, more background artifacts are present when Tikhonov regularization is used. This observation is most evident when Tikhonov regularization is used for both states, i.e. $\mathcal{R}_{\sigma_1} = \mathcal{R}_T$ and $\mathcal{R}_{\Delta\sigma} = \mathcal{R}_T$. On the other hand, when WS is used to estimate σ_1, reconstructions improve. Further yet, the most visually accurate reconstructions are realized when $\mathcal{R}_{\sigma_1} = \mathcal{R}_{WS}$ and $\mathcal{R}_{\Delta\sigma} = \mathcal{R}_{TV}$. This realization demonstrates the importance in using prior information to accurately estimate crack geometries. In this example, the use of prior information was encoded by spatial information in σ_1 via $\mathcal{R}_{WS}(\sigma_1)$ and sparsity of $\Delta\sigma$ via $\mathcal{R}_{TV}(\Delta\sigma)$. Intuitively, the reconstruction improvement in the former case – relative to the one-state reconstructions – is an expected result, since the two-state framework allows for appropriate prior models representing the physics of each state, the use of two data sets, and the proper use of constraints on each state. We note, however, that the improved resolution of the two-state framework results in doubling of the computational demand since both σ_1 and $\Delta\sigma$, having the same degrees of freedom, are simultaneously reconstructed. Such demand may be reduced by incorporating region of interest information, as discussed in (Liu et al. 2015a).

To investigate the computational behavior of the ERT reconstruction frameworks, we analyze the minimization behavior of the cost functionals for the one- and two-state problems, $\Psi_{ERT,1}$ and $\Psi_{ERT,2}$. Since the values of the

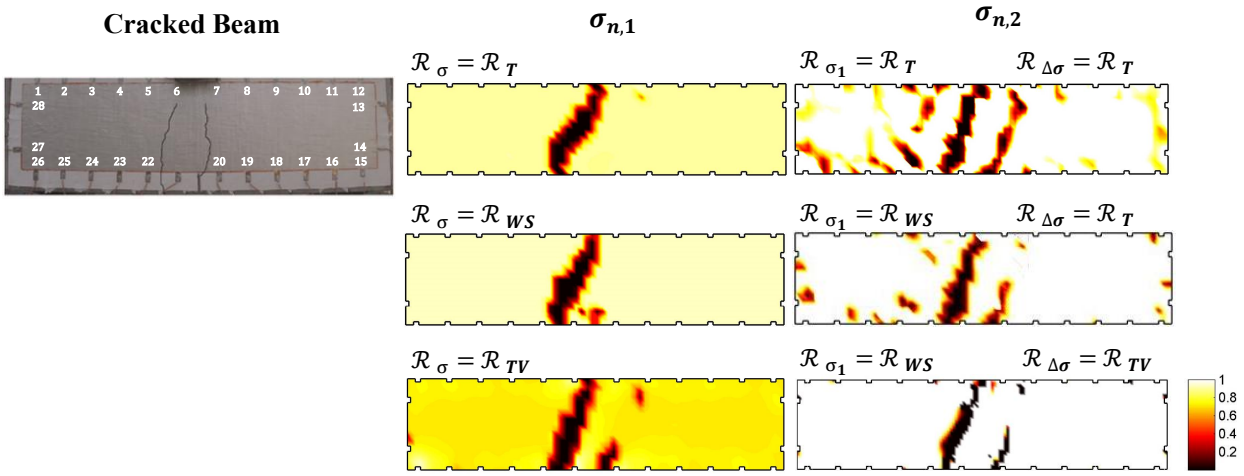

Figure 1. ERT imaging of a cracked reinforced concrete beam with an applied silver sensing skin: left column, photograph of the cracking pattern and electrode numbers shown in white. Middle column, one-state ERT reconstructions of the cracking pattern using Tikhonov, WS, and TV regularization denoted by $\mathcal{R}_\sigma = \mathcal{R}_T$, $\mathcal{R}_{WS}$, and $\mathcal{R}_{TV}$, respectively. Right column, two-state ERT reconstructions of the cracking pattern =using Tikhonov and WS regularization in estimating σ_1 and Tikhonov/TV regularization in estimating $\Delta\sigma$ (functionals for σ_1 and $\Delta\sigma$ denoted as $\mathcal{R}_{\sigma_1}$ and $\mathcal{R}_{\Delta\sigma}$). Images are normalized and the colorbar is unitless .

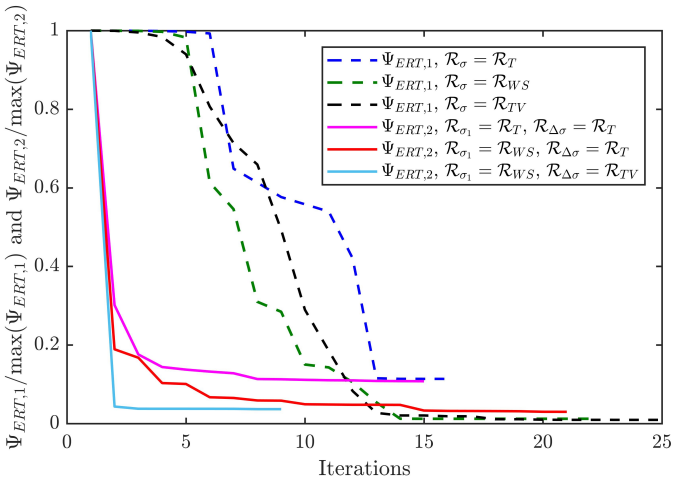

Figure 2. Minimization curves for one- and two-state ERT problems reporting normalized cost functionals, $\Psi_{ERT,1}/\max(\Psi_{ERT,1})$ and $\Psi_{ERT,2}/\max(\Psi_{ERT,2})$, respectively.

functionals vary by orders of magnitude (e.g. the data-discrepancy term in $\Psi_{ERT,2}$ is double that of $\Psi_{ERT,1}$ and different regularization functionals differ in magnitude), we plot the cost functionals normalized with respect to their maximum values. The normalized functionals are provided in Fig. 2. While all normalized functionals converge to similar values, we immediately observe two primary differences in one- and two-state functionals shown in Fig 2: (i) the drops in $\Psi_{ERT,1}$ are initially more gradual than those of $\Psi_{ERT,2}$ and (ii) as a whole, the one-state problems require more iterations to reach the stopping criteria. Observation (i) is explained by the poor initial guess for $\Delta\sigma = \mathbf{0}$, which is quite far from the final estimate, yet is quickly compensated for in the first iteration(s). The low iterations required to reach stopping criteria for the two-state problems, relative to the one-state problems, lies in the fact the the problems physics are more accurately captured using (a) physically-realistic constraints on each state and (b) prior knowledge of spatial properties inherent in σ_1 and $\Delta\sigma$ (when $\mathcal{R}_{WS}$ and $\mathcal{R}_{TV}$ are used), which cannot be fully captured using one-state frameworks.

QSEI imaging of damage in plates

In this subsection, we test the one- and two-state frameworks with application to QSEI of plate geometries. For both frameworks, we use simulated displacement data generated using the FEM forward model using a fine mesh with $N_{el} = 1,800$ three-node triangular elements. Following, we add Gaussian noise to the displacement data with 1% and 2% standard deviation and then interpolate the data onto a coarser mesh with $N_{el} = 450$ elements using linear interpolation to avoid an inverse crime. We note that this inverse problem was solved element-wise, resulting in a total of 450 degrees of freedom in E. Moreover, for computing the Jacobian, we utilized central differencing following Eq. 65. For the plate geometries, we use dimensionless units where the 10×10 plate has a uniform thickness of 0.1, a fixed left side, and a uniformly distributed load at on the right-hand side of 1 unit per unit length. Moreover, although the dimensions of the QSEI examples are unitless for demonstration purposes, the mean elastic modulus (near 300) and Poisson's ratio $\nu = 0.30$ were selected to reflect those of steel ($E = 200$ GPa and $\nu \approx 0.30$).

For the purposes of illustration, we begin by conducting one-state reconstructions of a narrow crack using the three forms of QSEI regularization $\mathcal{R}_E$ discussed in this article: Tikhonov, WS, and TV denoted as $\mathcal{R}_E = \mathcal{R}_T$, $\mathcal{R}_{WS}$, and $\mathcal{R}_{TV}$, respectively. The same regularization parameters in the previous section are also adopted here and the initial guess for the one-state QSEI problem is the homogeneous estimate $E = E_{\text{exp}}$. The ground truth and one-state reconstructions for noise levels of 1% and 2% are provided in Fig. 3. Note that, since the inverse problems in this subsection are solved in a piece-wise constant manner, the reconstructions are also shown as piece-wise constant.

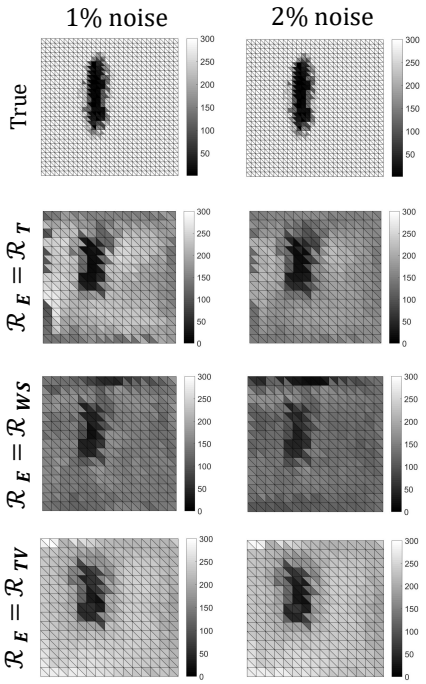

Figure 3. QSEI reconstructions of a narrow crack using Tikhonov, weighted smoothness (WS), and TV regularization using displacement data corrupted with 1% and 2% noise. The colorbars represent the unitless elastic modulus E.

Reconstructions in Fig. 3 support the feasibility of the one-state framework, using all three forms of regularization, for use in QSEI imaging in the presence of significant random noise, interpolation errors, and modeling errors. Indeed, in all the reconstructions the crack was localized, while reconstructions using TV and Tikhonov regularization provided the best images – which is expected, since both methods are known to be rather robust (Oberai et al. 2003). On the other hand, weighted smoothness did not perform as well at both noise levels and was a rather poor prior model selection. This is due to the unsuitability of weighted smoothness for detecting non-smoothly distributed inclusions.

To test the feasibility of the two-state frameworks in the context of QSEI, we consider a problem where the undamaged state E_1 is smoothly distributed and the damaged state has a simulated crack with the same geometry as in the one-state QSEI problems. We note here, however, that one-state solutions for QSEI problems with highly inhomogeneous backgrounds result in poor reconstruction quality (Smyl et al. 2018c) and is therefore not considered

herein. In solving the two-state QSEI problems, we use the same regularization functionals for $\mathcal{R}_{E_1}$ and $\mathcal{R}_{\Delta E}$ as those in the two-state ERT problems. Moreover, we use similar constraints as in the two-state ERT problem; namely, we set $\Psi_C^1 = \Psi_C^1(E_1 > 0)$, $\Psi_C^2 = \Psi_C^2(E_2 \geq 0)$, and $\Psi_C^3 = \Psi_C^3(\Delta E \leq 0)$, Reconstructions for this example are shown in Fig. 4.

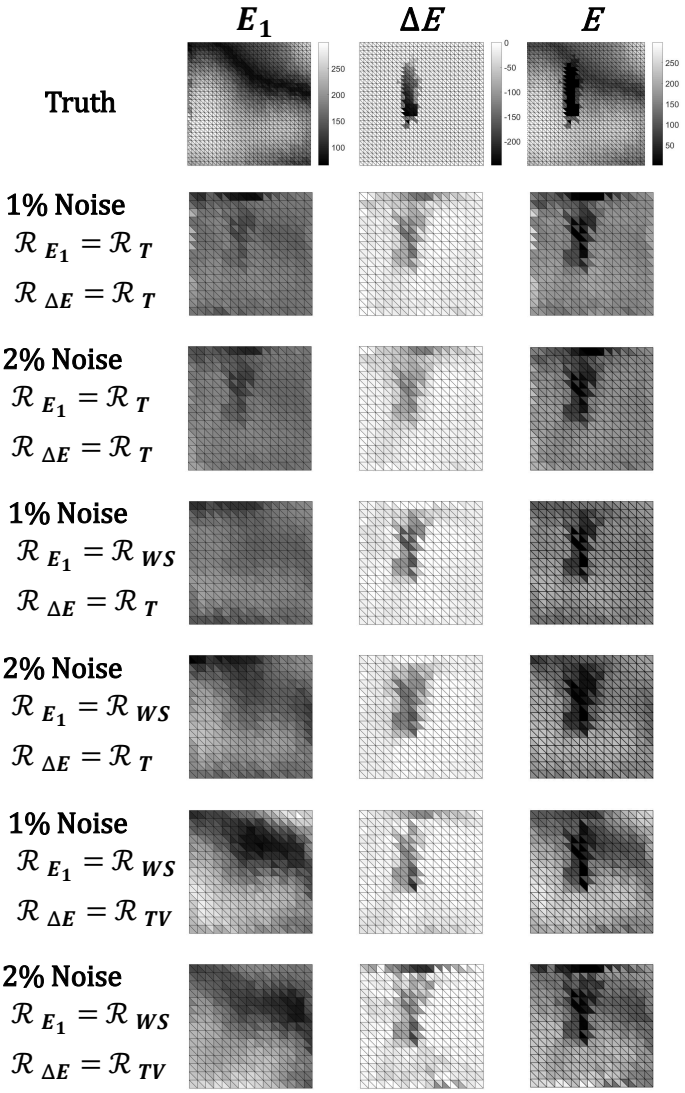

Figure 4. QSEI reconstructions of an inhomogeneous background and crack-like inclusion using the two-state framework considering noise levels of 1% and 2%: left column, true image and reconstructions of the background elastic modulus E_1; middle column, true image and reconstructions of the change in the elastic modulus due to localized damage ΔE; right column, true image and final estimates of $E = E_1 + \Delta E$. Reconstructions utilize Tikhonov regularization $\mathcal{R}_{E_1} = \mathcal{R}_T$ and weighted smoothness regularization $\mathcal{R}_{E_1} = \mathcal{R}_{WS}$ in estimating E_1 and Tikhonov regularization $\mathcal{R}_{\Delta E} = \mathcal{R}_T$ and TV regularization $\mathcal{R}_{\Delta E} = \mathcal{R}_{TV}$ in estimating ΔE.

Results shown in Fig. 4 clearly display that the two-state framework also works for QSEI. In all cases, the inclusion was accurately localized and the ellipsoidal shape was well captured. Moreover, the smooth distribution of E_1 was recognizably reconstructed, with the exception of the case where $\mathcal{R}_{E_1} = \mathcal{R}_T$. Indeed, we observe visible cross-talk in this case, mostly apparent in E_1 reconstructions, which results from using the uninformative prior model $\mathcal{R}_T$ in estimating E_1. This illustrates that the use of physically-realistic constraints is not always sufficient in preventing cross-talk between states E_1 and ΔE (or in parameterizations θ_1 and $\Delta\theta$, in general). Lastly, as in the two-state ERT

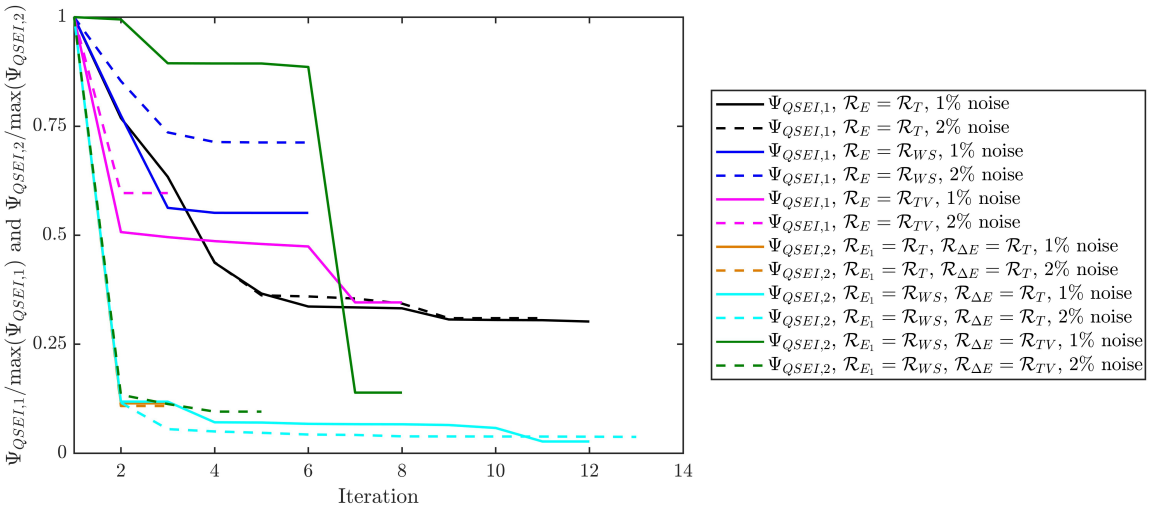

Figure 5. Minimization curves for one- and two-state QSEI problems reporting normalized cost functionals, $\Psi_{QSEI,1}/\max(\Psi_{QSEI,1})$ and $\Psi_{QSEI,2}/\max(\Psi_{QSEI,2})$, respectively.

example, we again visually observe that images of undamaged and damaged states are most accurately reconstructed what structural prior information is incorporated in regularization schemes for both states.

In addition to the visual quality of the QSEI reconstructions, we are also interested in the iterative minimization behavior of the QSEI reconstructions. Similar to the previous subsection, the normalized cost functionals for the one-state and two-state QSEI reconstructions are provided in Fig. 5. Immediately, we observe the large differences in the minimization behavior between the one- and two-state frameworks: namely that, despite the notably more difficult problem in simultaneously reconstructing two parameter fields (E_1 and ΔE), the two-state functionals consistently reach a lower minimum than the one-state functionals. This observation is in contrast with the one- and two-state ERT functionals, which reached comparable normalized minimum values. This result may indicate that QSEI is more sensitive than ERT to the way in which the inverse problem is parameterized. Some possible explanations for this include, (i) high susceptibility to errors induced via interpolation of data to a coarse mesh, (ii) reconstruction improvement via error absorption in E_1 reconstructions, (iii) differing degrees of modeling errors in QSEI and ERT forward models, and (iv) differing sensitivity of the parameter field to input data (i.e. differences in ill-posedness between the QSEI and ERT inverse problems).

Joint ERT/QSEI imaging of damage in plates

In this subsection, we aim to demonstrate the feasibility of a joint framework with a structural operator for simultaneous ERT and QSEI reconstruction of a discrete crack numerically. We begin by observing the form of Eq. 70 and note that the magnitudes of the data norm, regularization functional, and constraint functional may differ by orders of magnitude. While Eq. 70 is certainly feasible for joint reconstruction, we observed that, due to the large differences in functional magnitudes, results were generally more reliable with less visual artifacts when the cost functional was modified by taking the base 10 logarithm of each component and adding positivity constraint as follows

$$\Psi_{\mathcal{J},E/Q} = \log_{10}(||L_{\mathcal{J}}(\mathcal{D}_{\mathcal{J}} - U_{\mathcal{J}}(\Theta_{\mathcal{J},E/Q}))||^2) + \log_{10}(\mathcal{R}_{\mathcal{J}}(\Theta_{\mathcal{J},E/Q})) + \log_{10}(\kappa_C \Psi_C) + \log_{10}(\kappa \Psi_{\mathfrak{C}}) \quad (74)$$

where $\kappa_C = 10^{-3}$, $\kappa = 1.0$, and the threshold parameter $\tau = 0.1$ were selected. For regularization, TV was utilized, $\alpha_{TV} = 6 \times 10^{-3}$ and $\beta = 160$ were used for both ERT and QSEI reconstructions. Since no information on joint ERT/QSEI imaging is available in the literature, these parameters were selected on the basis of trial and error. To corroborate the joint approach, we compare joint results with a dual problem, namely, simultaneously reconstructing E and σ by simply adding the cost functions provided in Eqs. 55 and 61 and separately solving each minimization in the same Gauss-Newton loop with different search directions and steps. The resulting dual problem cost functional is the written as $\Psi_D = \Psi_{ERT,1} + \Psi_{QSEI,1}$.

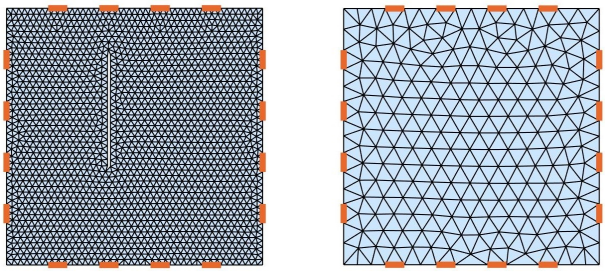

Figure 6. Discretizations used for (a) simulating joint ERT/QSEI data and (b) solving the joint inverse problem. ERT electrodes are shown in red.

For both the joint and dual problems, we use the same 10×10 unitless data simulation and inverse meshes shown in Fig. 6a and 6b for the QSEI and ERT problems, respectively. The target 4×0.12 unit length crack was modeled as a discontinuous inclusion in the fine mesh using six node triangles with quadratic basis functions and $N_{el} = 3,653$ and $N_n = 7,515$ elements and nodes. The inverse mesh, on the other hand, uses a continuous mesh with the same order triangles and $N_{el} = 423$ and $N_n = 904$ elements and nodes. The selection of the higher-order triangles and discontinuous mesh was done to (i) test the efficacy of joint reconstructions employing higher order hpk elements (Surana and Reddy 2016), (ii) test the regimes' robustness to added modeling uncertainties – in addition to the standard 1.0% noise commonly used in ERT and QSEI reconstructions, and (iii) demonstrate the simulated ERT/QSEI data may be generated by means other than setting $E \approx 0$ or $\sigma \approx 0$ at the target location (as is commonly done). Moreover, we investigate a node-wise solution to the QSEI problem (rather than element-wise), which doubles the degrees of freedom in E relative to the three-node triangular meshing. This also increases the computational demand by roughly a factor of 4. This is due to the increased degrees of freedom by solving the problem node wise, thereby significantly increasing the time required to compute a pertubed Jacobian. We therefore utilize the Jacobian computation technique used in (Vilhunen et al. 2002), requiring only one forward solution per iteration, rather than the perturbation method with central differencing requiring $2N_n$ solves of the forward model.

To simulate the ERT data, 16 equally spaced electrodes were used and a unitless homogeneous background conductivity $\sigma = 10$ was considered. A total of 16 direct current injections were applied between electrodes i and j, $i = 1, 5, 9, 13$ and $j = 1, ..., 16, i \neq j$. Corresponding to each current injection, 225 adjacent electrode potentials were measured. In simulating the QSEI data, a uniform tensile force of 1 unit/length was applied to the right side of the geometries with a homogeneous and unitless background $E = 10$, while the left side was fixed. The same displacement field interpolation scheme for interpolating the simulated data to the inverse mesh used in section was also used here.

Reconstructions for the dual and joint problems are shown in Figs. 7a and 7b, respectively. Images shown in Fig. 7 clearly localize the crack location and capture the crack angle for both the dual and joint approaches, supporting the feasibility of both frameworks. Interestingly, ERT reconstructions are visually most accurate. The improved resolution in ERT images largely results from the fact that added interpolation error is not present in ERT measurements, which also explains the smoothness in QSEI crack reconstructions.

As a whole, the joint reconstructions with a structural operator are only slightly better that the dual problem reconstructions. This observation is supported by Fig. 8, reporting the normalized drops in the cost functionals and an overall lower normalized minimum in the joint cost function relative to the dual problem. Moreover, the drops in the cost functionals for the dual and joint problems decrease only slightly before the the functionals increase, which resulted in termination of the algorithm and storing of the previous iteration as the final estimate. There are numerous potential reasons for the observed behavior of the dual and joint problems, which highlight some challenges in dual/joint inverse problems. Some common factors contributing to the challenges in joint problems are discussed in the following itemization:

- The use of coupled regularization. The regularization scheme used in this approach was selected based on the physical realization that the crack is sharp and TV regularization is therefore a natural choice. However, the choice of dependent variables in β and α_{TV} were static for ERT and QSEI, i.e. they did not change at each iteration. Moreover, the selection was done by trial and error and is therefore not optimal. Better selection

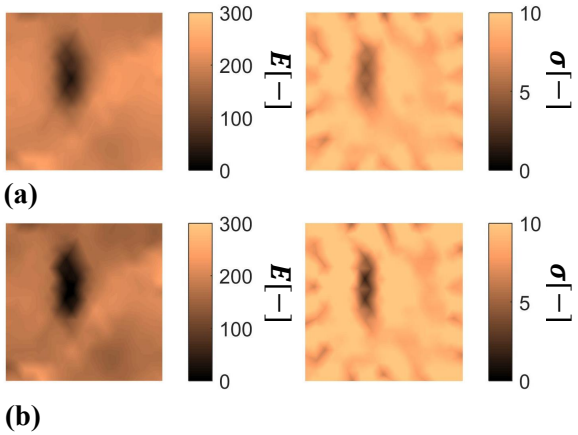

Figure 7. QSEI (left column) and ERT (right column) reconstructions for the (a) dual problem and (b) joint problem with a structural operator. Reconstructed parameters σ and E are unitless.

of these parameters may be conducted by taking into account the noise level, relative tradeoffs with the data discrepency norm, convergence rate of the joint cost functional, etc. (Holler et al. 2018).

- Selection of a structural operator $\Psi_{\mathfrak{C}}$. There are countless possible choices for $\Psi_{\mathfrak{C}}$, which may have a significant effect on the reconstruction quality; for example, one may chose functional proportionality to the gradient of the normalized parameter field $\mathfrak{C}(\vartheta_n) \propto \mathfrak{C}(\nabla\vartheta_n)$, the curvature of the normalized parameter field $\mathfrak{C}(\vartheta_n) \propto \mathfrak{C}(\nabla^2\vartheta_n)$ (Haber and Oldenburg 1997), or a combination $\mathfrak{C}(\vartheta_n) \propto \mathfrak{C}(\nabla^2\vartheta_n + \nabla\vartheta_n + \vartheta_n)$. Often, a smoothing function $\mathfrak{F}$ is applied to the parameter field $\mathfrak{C}(\vartheta_n) \propto \mathfrak{F}(\nabla^2\vartheta_n + \nabla\vartheta_n + \vartheta_n)$, which may improve the numerical behavior by avoiding saw-tooth instabilities resulting from sudden drops in $\Psi_{\mathfrak{C}}$.
- Choosing the threshold τ. At present, the optimized selection of a static τ for joint ERT/QSEI reconstruction is ambiguous. Intuitively, one may wish to select $\tau = 0.5$ as a first approximation. In our analysis, however, we found that $\tau = 0.5$ led to significantly over-penalized and over-smoothed reconstructions. By decreasing τ, reconstruction sharpness improved and reconstructions were more robust to changes in regularization parameters. One should use this observation with some caution when selecting more complicated structural operators. On the other hand, τ may selected at each iteration, by sweeping through representative values such that the lowest cost functional is minimized.
- Selection of structural operator and constraint weighting coefficients κ and κ_C. This issue was somewhat circumvented by taking the logarithm of each component in Eq. 74, essentially scaling the component functionals to values ranging from 1 - 8, rather than the disproportional 10 - 10^8. This is a a rather rudimentary technique, where more advanced scaling of κ and κ_C may be chosen iteratively or statically, based on a suite of parameters, such as the noise level, choice of regularization, convergence, etc. (Matthews and Anastasio 2017)

Despite the present challenges in joint ERT/QSEI imaging, which, to the authors' knowledge was first proposed/addressed herein, joint ERT/QSEI imaging was effective in localizing damage in distributions of both σ and E. Moreover, the joint framework is promising, in that, it doubles the information given by tomography – which may be used in a complimentary or independent manner. In future research, optimization of regularization parameters, $\Psi_{\mathfrak{C}}$, τ, and the weighting coefficients in joint frameworks will be further investigated.

Recommendations for implementing damage tomography frameworks

In this section, we provide basic recommendations for implementing structural damage tomography frameworks. We begin by providing a brief tutorial for first-time users implementing damage tomography. Owing to the complexities of solving stationary damage tomography problems in general, we include only essential aspects required for new users to implement one-state least-squares based damage tomography. Following, we concisely provide general recommendations for implementing damage tomography frameworks.

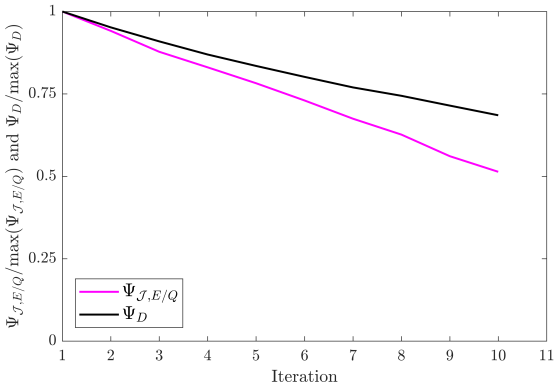

Figure 8. Minimization curves for the dual and joint problems, the cost functionals are denoted by Ψ_D and $\Psi_{\mathcal{J},E/Q}$, respectively.

Approaching damage tomography for the first time

For users who are new to damage tomography, the initial coding of a damage tomography algorithm can be a daunting task. For this health reasons, we recommend that the user begin their journey with the most simple framework: one-state tomography. One way of approaching this task is to list the bare minimum function requirements needed to solve a least-squares based damage tomography problem:

1. Forward model
2. Cost function
3. Jacobian
4. Linesearch
5. Iterative loop including a stopping criteria

Although all items in the enumeration are essential, item (1) is possibly the most important for first implementations. This is especially true when experimental data d is used, since the forward model needs to accurately represent the problem physics. Luckily, in many cases, open source FEM software is readily available. In implementing such software, users should take note that the majority of open-source FEM software solves problems where the parameter field is homogeneous – therefore, the user will generally need to write a loop to update the inhomogeneous parameter field at each iteration.

After the user has acquired a forward model U, the user will then need to decide exactly which tomography problem he/she would like to solve. For the very first implementation we recommend solving a Tikhonov regularized least squares problem without weighting (adding the weighting matrix W is very straight forward). Using the same nomenclature as in previous sections for estimating a parameter θ, the least squares update would be written explicitly as

$$\bar{\theta} = (J^T J + \Gamma_T^{-1})^{-1}(J^T(d - U(\theta_{k-1})) \tag{75}$$

where $\alpha_T = 10^{-3}$ is a recommended starting point for the Tikhonov regularization parameter in Γ_T and the Jacobian J, updated at each iteration k, can most simply be computed using Eq. 66 (obviously substituting the correct parameter θ_{k-1}).

Moreover, since the problem is solved iteratively, the user will need to make an initial guess for $\theta_{k=1}$. For this, one could use the best homogeneous guess (recommended) or simply make a guess based on an a reasonable expected value. Now that the user has a sketch of the least squares problem, he/she will need to write down the corresponding cost functional. Since weighting is not used at this point, the cost functional may be written simply as

$$\Psi = ||d - U(\theta)||^2 + ||\Gamma_T \theta||^2. \tag{76}$$

The last items required are a linesearch and an iterative loop with some stopping criteria. For the linesearch, which is required to ensure Ψ is maximally decreasing at each step, the user may simply write a function which searches for the step length s_k which minimizes $\Psi(\theta_{k-1} + s_k\bar{\theta})$ in a trust region, for example (0,2). It is important to remark here

that since we generally assume $\theta > 0$, we need to ensure this to avoid numerical problems with U (such as complex numbers). For the purposes of a first attempt at tomography, the projection method may be used, where we simply project values of $\theta < 0$ such that $\theta > r$ where r is a small number (e.g. 10^{-4}). In writing the iterative loop, there are three primary items to consider: (i) that $\bar{\theta}$, J, and s_k are updated at each iteration, (ii) θ_k and Ψ_k are stored at each iteration, and that (iii) the the program is terminated once a stopping criteria is reached. There are many examples for a stopping criteria; we recommend a simple form, such as ($\Psi_{k-1} - \Psi_k < \text{tol}$ *or* $\Psi_k > \Psi_{k-1}$) where tol is a sufficiently small number. To summarize this algorithmic components discussed in this subsection, pseudocode is provided in Algorithm 1.

Data: d, resulting from (a) experiment or (b) noisy simulations utilizing U
Result: Damage tomography, reconstructing parameter θ
initialize $\theta_{k=1}$, $\Psi_{k=1}$,maxiterations, $\Gamma_T = \alpha_T I$, r, tol;
for *k = 2:*maxiterations **do**
  Compute J;
  Compute $\bar{\theta} = (J^T J + \Gamma_T^{-1})^{-1}(J^T(d - U(\theta_{k-1}))$;
  Find s_k using linesearch by solving: min($\Psi(\theta_{k-1} + s_k\bar{\theta})$);
  Update solution: $\theta_k = \theta_{k-1} + s_k\bar{\theta}$;
  Project $\theta_k < 0$ to ensure $\theta_k > r$;
  Compute $\Psi_k(\theta_k)$;
  Store Ψ_k and θ_k;
  if $\Psi_{k-1} - \Psi_k < \text{tol}$ or $\Psi_k > \Psi_{k-1}$ **then**
    Break
  end
end

Algorithm 1: Generic pseudocode for first-time users of damage tomography aiming to reconstruct the parameter field θ.

General recommendations and potential pitfalls

The primary motivation for providing one-state, two-state, and joint frameworks that may be parameterized/constrained/regularized in a flexible and combinatory manner is to promote creative solutions, potentially improving reconstructions obtained using damage tomography. However, it is the experience of the authors that, simply increasing the complexity of the tomographic approach does not necessarily yield better reconstructions than simple regimes. In the following, we concisely list some practical recommendations and potential pitfalls in implementing the damage tomography frameworks derived in this article and general recommendations related to damage tomography functionalities in general.

1. *Increasing the degrees of freedom in the inverse problem does not guarantee improvements in reconstructions.* While increasing the degrees of freedom in a numerical forward model often lowers the error in, e.g., FEM forward models, the same is not always true for inverse problems. In fact, by increasing the degrees of freedom, not only does the inverse problem become more computationally demanding, the size of the solution space may also increase (Benning and Burger 2018).
2. *Use prior knowledge whenever possible.* Prior knowledge, often associated with the way a parameter field is regularized, may also be incorporated in the implementation of constraints, selection of framework parameterization, selection of regularization schemes, error approximation, and much more. Often, simply considering the problem physics, especially regarding how the state of the parameter field changes before and after damage, offers significant prior information.
3. *Begin solving damage tomography problems using the most simplistic model first.* Often, one-state solutions offer sufficient resolution for the task at hand. Implementing two-state and joint regimes is time intensive (coding), computationally demanding, and should only be considered if the results from one-state solutions are insufficient.
4. *In general, projection – alone – is not sufficient.* This pitfall is subtle and is often not considered until the user has issues deciphering why the problem is not behaving as expected. Applying a positivity constraint by only

projecting values such that the parameter field is greater than 0, e.g. $\theta > 0$, can lead to problems. As a rule of thumb, the constraint gradient(s) and Hessian(s) should always be included in the least-squares update.

5. *Terms in the least-squares updates should be be reflected in the cost functional.* This may seem like common sense, however, a lot of heartache can be avoided if terms in the least-squares update (related to constraints, regularization, etc.) are properly reflected in the cost function. This comment is increasingly important as the complexity of the framework increases and terms are possibly lost due to human error.
6. *More data does not always improve reconstruction quality.* This comment is somewhat counter-intuitive. However, in some cases, especially in cases where successive data sets were collected using different means, noise models that worked for one data set may not work as well for others – in such cases simply adding more data may actually degrade reconstruction quality. For example, data set one may have Gaussian-distributed noise, where data set two has Poisson noise. As another example, using a expected noise variance (a) for data one and noise variance (a) for data two may not be sufficient some cases. We note however, that this phenomenon is not common in our experience and should not be the first consideration when tailoring a tomographic framework
7. *Visualization is an powerful tool in understanding problem behavior.* It is certainly gratifying to observe accurate reconstructions of damage when the solution framework is fully functional. However, much of solving inverse problems involves attempting to understand why the algorithm *is not* working and debugging. For this purpose, it is helpful to plot and visualize aspects such as: the data fidelity (e.g., real data d vs. $U(\theta)$), the rate at which the cost function is being minimized, and updated reconstructions at each iteration.
8. *Starting "from scratch" is not necessary.* There are many open source tomographic regimes available, which may serve as a starting point, benchmark, or reference for new users. Some open source options include: EIDORS (ERT) (Adler and Lionheart 2006), open source D-Bar for ERT (with experimental data) (Hauptmann et al. 2017), OpenQSEI (QSEI) (Smyl et al. 2018b), Ncorr (DIC) (Blaber et al. 2015), and more.

Conclusions

This article focused on the development of straightforward frameworks for stationary tomography of structural damage. In this effort, we provided 38 tomographic frameworks for one-state, two-state, and joint imaging of structural damage. The frameworks were based on least-squares inverse methods and are adaptable for incorporating different regularization, constraints, and structural models based on realization of the problem physics. To give insight into potential practical applications, the frameworks were applied to two emerging structural imaging modalities, Electrical Resistance Tomography (ERT) and Quasi-Static Elasticity Imaging (QSEI). Following, selected frameworks were employed to test their feasibility to image damage in structural members using experimental- and numerically-obtained data. Lastly, a primer for first-time users of the damage tomography framework and recommendations/potential pitfalls in using the proposed frameworks were discussed.

ERT, QSEI, and joint ERT/QSEI frameworks were shown to be effective in detecting damage, especially in the case of discrete cracking. In doing this, it was also demonstrated that the frameworks were robust to considerable levels of random measurement noise, interpolation errors, and modeling errors. In the case of joint ERT/QSEI tomography, a novel imaging regime, the images showed moderate artifacts and over smoothing. The causes of these discrepancies were found to result primarily from non-optimization of coupled regularization parameters, a simplistic structural operator, the selection of the threshold parameter, and rudimentary nature of weighting component functionals within the joint cost functional. Despite the present shortfalls, joint ERT/QSEI imaging offers double the structural information than individual tomographic regimes and therefore has significant potential for stationary tomography of structural damage.

Acknowledgments

DS, SB, WA, and AV would like to acknowledge the support of the Department of Mechanical Engineering at Aalto University throughout this project. DS, SB, WA, and AV would also like to acknowledge funding from the European Research Council under the European Union's Seventh Framework Programme (FP7/2007-2013) / ERC grant agreement n339380. DL was supported by the National Natural Science Foundation of China under Grant No. 61871356 and Anhui Provincial Natural Science foundation under Grant 1708085MA25, this support is greatly acknowledged.

References

Adler A and Lionheart WR (2006) Uses and abuses of EIDORS: an extensible software base for EIT. *Physiol. Meas.* 27(5): S25.

Adler J and Öktem O (2017) Solving ill-posed inverse problems using iterative deep neural networks. *Inverse Problems* 33(12): 124007.

Aithal R and Saigal S (1995) Shape sensitivity analysis in thermal problems using bem. *Engineering analysis with boundary elements* 15(2): 115–120.

An HB, Wen J and Feng T (2011) On finite difference approximation of a matrix-vector product in the jacobian-free newton–krylov method. *Journal of Computational and Applied Mathematics* 236(6): 1399 – 1409.

Aster RC, Borchers B and Thurber CH (2018) *Parameter estimation and inverse problems*. Elsevier.

Balageas D, Fritzen CP and Güemes A (2010) *Structural health monitoring*, volume 90. John Wiley & Sons.

Benning M and Burger M (2018) Modern regularization methods for inverse problems. *Acta Numerica* 27: 1–111.

Blaber J, Adair B and Antoniou A (2015) Ncorr: open-source 2d digital image correlation matlab software. *Experimental Mechanics* 55(6): 1105–1122.

Bonnet M, Burczyński T and Nowakowski M (2002) Sensitivity analysis for shape perturbation of cavity or internal crack using bie and adjoint variable approach. *International Journal of Solids and Structures* 39(9): 2365–2385.

Bonnet M and Constantinescu A (2005) Inverse problems in elasticity. *Inverse problems* 21(2): R1.

Cha YJ and Buyukozturk O (2015) Structural damage detection using modal strain energy and hybrid multiobjective optimization. *Computer-Aided Civil and Infrastructure Engineering* 30(5): 347–358.

Cha YJ, Choi W, Suh G, Mahmoudkhani S and Büyüköztürk O (2017) Autonomous structural visual inspection using region-based deep learning for detecting multiple damage types. *Computer-Aided Civil and Infrastructure Engineering* .

Chen Y, O'Sullivan JA, Politte DG, Evans JD, Han D, Whiting BR and Williamson JF (2016) Line integral alternating minimization algorithm for dual-energy x-ray ct image reconstruction. *IEEE transactions on medical imaging* 35(2): 685–698.

Cheng KS, Isaacson D, Newell J and Gisser D (1989) Electrode models for electric current computed tomography. *IEEE T. Bio-Med. Eng.* 36(9): 918–924.

Corr D, Accardi M, Graham-Brady L and Shah S (2007) Digital image correlation analysis of interfacial debonding properties and fracture behavior in concrete. *Engineering Fracture Mechanics* 74(1-2): 109–121.

Dai H, Gallo GJ, Schumacher T and Thostenson ET (2016) A novel methodology for spatial damage detection and imaging using a distributed carbon nanotube-based composite sensor combined with electrical impedance tomography. *Journal of Nondestructive Evaluation* 35(2): 1–15.

Ehrhardt MJ, Thielemans K, Pizarro L, Atkinson D, Ourselin S, Hutton BF and Arridge SR (2014) Joint reconstruction of pet-mri by exploiting structural similarity. *Inverse Problems* 31(1): 015001.

Fan W and Qiao P (2011) Vibration-based damage identification methods: a review and comparative study. *Structural health monitoring* 10(1): 83–111.

Farrar CR and Worden K (2012) *Structural health monitoring: a machine learning perspective*. John Wiley & Sons.

Gallo GJ and Thostenson ET (2016) Spatial damage detection in electrically anisotropic fiber-reinforced composites using carbon nanotube networks. *Composite Structures* 141: 14–23.

Gangadharan R, Murthy C, Gopalakrishnan S and Bhat M (2009) Time reversal technique for health monitoring of metallic structure using lamb waves. *Ultrasonics* 49(8): 696–705.

Garde H and Staboulis S (2017) Convergence and regularization for monotonicity-based shape reconstruction in electrical impedance tomography. *Numerische Mathematik* 135(4): 1221–1251.

Gebauer B and Hyvönen N (2007) Factorization method and irregular inclusions in electrical impedance tomography. *Inverse Problems* 23(5): 2159.

Gillich GR and Praisach ZI (2014) Modal identification and damage detection in beam-like structures using the power spectrum and time–frequency analysis. *Signal Processing* 96: 29–44.

González G, Kolehmainen V and Seppänen A (2017) Isotropic and anisotropic total variation regularization in electrical impedance tomography. *Computers & Mathematics with Applications* 74(3): 564–576.

Greenleaf A, Kurylev Y, Lassas M and Uhlmann G (2009) Invisibility and inverse problems. *Bulletin of the American Mathematical Society* 46(1): 55–97.

Haber E and Oldenburg D (1997) Joint inversion: a structural approach. *Inverse problems* 13(1): 63.

Hallaji M, Seppänen A and Pour-Ghaz M (2014) Electrical impedance tomography-based sensing skin for quantitative imaging of damage in concrete. *Smart Mater. Struct.* 23(8): 085001.

Hansen PC (2005) *Rank-deficient and discrete ill-posed problems: numerical aspects of linear inversion*, volume 4. Siam.

Hartley HO (1961) The modified gauss-newton method for the fitting of non-linear regression functions by least squares. *Technometrics* 3(2): 269–280.

Hauptmann A, Kolehmainen V, Mach NM, Savolainen T, Seppänen A and Siltanen S (2017) Open 2d electrical impedance tomography data archive. *arXiv preprint arXiv:1704.01178* .

Hejll A (2004) *Structural health of bridges: monitor, assess and retrofit*. PhD Thesis, Luleå tekniska universitet.

Holler M, Huber R and Knoll F (2018) Coupled regularization with multiple data discrepancies. *Inverse Problems* 34(8): 084003.

Isaacson D (1986) Distinguishability of conductivities by electric current computed tomography. *IEEE transactions on medical imaging* 5(2): 91–95.

Isaacson D, Mueller J, Newell J and Siltanen S (2006) Imaging cardiac activity by the d-bar method for electrical impedance tomography. *Physiological Measurement* 27(5): S43.

Jafarkhani R and Masri SF (2011) Finite element model updating using evolutionary strategy for damage detection. *Computer-Aided Civil and Infrastructure Engineering* 26(3): 207–224.

Kaipio J and Somersalo E (2005) *Statistical and Computational Inverse Problems*. Springer New York.

Kang J, Ososkov Y, Embury JD and Wilkinson DS (2007) Digital image correlation studies for microscopic strain distribution and damage in dual phase steels. *Scripta Materialia* 56(11): 999–1002.

Karhunen K, Seppänen A, Lehikoinen A, Monteiro PJ and Kaipio JP (2010) Electrical resistance tomography imaging of concrete. *Cement and Concrete Res.* 40(1): 137–145.

Knudsen K, Lassas M, Mueller JL and Siltanen S (2009) Regularized d-bar method for the inverse conductivity problem. *Inverse Problems and Imaging* 35(4): 599.

Kong X and Li J (2018a) Image registration-based bolt loosening detection of steel joints. *Sensors* 18(4): 1000.

Kong X and Li J (2018b) Vision-based fatigue crack detection of steel structures using video feature tracking. *Computer-Aided Civil and Infrastructure Engineering* .

Küntz M, Jolin M, Bastien J, Perez F and Hild F (2006) Digital image correlation analysis of crack behavior in a reinforced concrete beam during a load test. *Canadian Journal of Civil Engineering* 33(11): 1418–1425.

Lassas M and Siltanen S (2004) Can one use total variation prior for edge-preserving bayesian inversion? *Inverse Problems* 20(5): 1537.

Lefkimmiatis S, Bourquard A and Unser M (2012) Hessian-based norm regularization for image restoration with biomedical applications. *IEEE Transactions on Image Processing* 21(3): 983–995.

Liu D, Kolehmainen V, Siltanen S, Laukkanen A and Seppänen A (2015a) Estimation of conductivity changes in a region of interest with electrical impedance tomography. *Inverse Probl. Imag.* 9(1): 211–229.

Liu D, Kolehmainen V, Siltanen S, Laukkanen AM and Seppänen A (2016) Nonlinear difference imaging approach to three-dimensional electrical impedance tomography in the presence of geometric modeling errors. *IEEE Trans. Biomed. Engineering* 63(9): 1956–1965.

Liu D, Kolehmainen V, Siltanen S and Seppänen A (2015b) A nonlinear approach to difference imaging in EIT; assessment of the robustness in the presence of modelling errors. *Inverse Problems* 31(3): 035012.

Liu P and Zheng J (2010) Recent developments on damage modeling and finite element analysis for composite laminates: A review. *Materials & Design* 31(8): 3825–3834.

LLorca J, González C, Molina-Aldareguía JM, Segurado J, Seltzer R, Sket F, Rodríguez M, Sádaba S, Muñoz R and Canal LP (2011) Multiscale modeling of composite materials: a roadmap towards virtual testing. *Advanced Materials* 23(44): 5130–5147.

Malitckii E, Remes H, Lehto P, Yagodzinskyy Y, Bossuyt S and Hänninen H (2018) Strain accumulation during microstructurally small fatigue crack propagation in bcc fe-cr ferritic stainless steel. *Acta Materialia* 144: 51–59.

Matthews TP and Anastasio MA (2017) Joint reconstruction of the initial pressure and speed of sound distributions from combined photoacoustic and ultrasound tomography measurements. *Inverse problems* 33(12): 124002.

Mellings S and Aliabadi M (1995) Flaw identification using the boundary element method. *International Journal for Numerical Methods in Engineering* 38(3): 399–419.

Moradi S, Razi P and Fatahi L (2011) On the application of bees algorithm to the problem of crack detection of beam-type structures. *Computers & Structures* 89(23-24): 2169–2175.

Mueller J and Siltanen S (2012) *Linear and Nonlinear Inverse Problems with Practical Applications*. SIAM.

Nguyen VP, Lloberas-Valls O, Stroeven M and Sluys LJ (2011) Homogenization-based multiscale crack modelling: from micro-diffusive damage to macro-cracks. *Computer Methods in Applied Mechanics and Engineering* 200(9-12): 1220–1236.

Niinimaki K, Lassas M, Hamalainen K, Kallonen A, Kolehmainen V, Niemi E and Siltanen S (2016) Multiresolution parameter choice method for total variation regularized tomography. *SIAM Journal on Imaging Sciences* 9(3): 938–974.

Nishimura N (1995) Applications of boundary integral equation method to various crack determination problems. *Dynamic fracture mechanics(A 96-14151 02-39), Southampton, United Kingdom and Billerica, MA, Computational Mechanics Publications, 1995,* : 285–311.

Nissinen A, Heikkinen L and Kaipio J (2007) The bayesian approximation error approach for electrical impedance tomography—experimental results. *Measurement Science and Technology* 19(1): 015501.

Oberai AA, Gokhale NH and Feijóo GR (2003) Solution of inverse problems in elasticity imaging using the adjoint method. *Inverse problems* 19(2): 297.

Oberkampf WL, DeLand SM, Rutherford BM, Diegert KV and Alvin KF (2002) Error and uncertainty in modeling and simulation. *Reliability Engineering & System Safety* 75(3): 333–357.

Ou J and Li H (2010) Structural health monitoring in mainland china: review and future trends. *Structural Health Monitoring* 9(3): 219–231.

Paget CA, Grondel S, Levin K and Delebarre C (2003) Damage assessment in composites by lamb waves and wavelet coefficients. *Smart materials and Structures* 12(3): 393.

Pan B, Qian K, Xie H and Asundi A (2009) Two-dimensional digital image correlation for in-plane displacement and strain measurement: a review. *Measurement science and technology* 20(6): 062001.

Park HW, Sohn H, Law KH and Farrar CR (2007) Time reversal active sensing for health monitoring of a composite plate. *Journal of Sound and Vibration* 302(1-2): 50–66.

Perera R, Fang SE and Ruiz A (2010) Application of particle swarm optimization and genetic algorithms to multiobjective damage identification inverse problems with modelling errors. *Meccanica* 45(5): 723–734.

Rashetnia R, Alla OK, Gonzalez-Berrios G, Seppanen A and Pour-Ghaz M (2018) Electrical resistance tomography–based sensing skin with internal electrodes for crack detection in large structures. *Materials Evaluation* 76(10): 1405–1413.

Reynders E and De Roeck G (2010) A local flexibility method for vibration-based damage localization and quantification. *Journal of sound and vibration* 329(12): 2367–2383.

Rose JL (2014) *Ultrasonic guided waves in solid media*. Cambridge university press.

Rose L and Wang C (2004) Mindlin plate theory for damage detection: Source solutions. *The Journal of the Acoustical Society of America* 116(1): 154–171.

Salawu O (1997) Detection of structural damage through changes in frequency: a review. *Engineering structures* 19(9): 718–723.

Schmitt S (2009) The factorization method for eit in the case of mixed inclusions. *Inverse Problems* 25(6): 065012.

Seppänen A, Hallaji M and Pour-Ghaz M (2014a) Electrical impedance tomography-based sensing skin for detection of damage in concrete. In: *Proceedings of the 11th European Conference on Non-Destructive Testing (ECNDT 2014), Prague, Czech Republic*. pp. 6–10.

Seppänen A, Hallaji M and Pour-Ghaz M (2014b) Electrical impedance tomography-based sensing skin for detection of damage in concrete. In: *11th European Conference on Non-Destructive Testing (ECNDT 2014)*. Prague, Czech Republic.

Smyl D, Antin KN, Liu D and Bossuyt S (2018a) Coupled digital image correlation and quasi-static elasticity imaging of inhomogeneous orthotropic composite structures. *Inverse Problems* 34(12): 124005.

Smyl D, Bossuyt S and Liu D (2018b) Openqsei: a matlab package for quasi static elasticity imaging. *arXiv preprint arXiv:1802.09349* .

Smyl D, Bossuyt S and Liu D (2018c) Stacked elasticity imaging approach for visualizing defects in the presence of background inhomogeneity. *Journal of Engineering Mechanics* : doi: 10.1088/0964–1726/23/4/045034.

Smyl D, Pour-Ghaz M and Seppänen A (2018d) Detection and reconstruction of complex structural cracking patterns with electrical imaging. *NDT & E International* 99: 123–133.

Smyl D, Rashetnia R, Seppänen A and Pour-Ghaz M (2017) Can electrical resistance tomography be used for imaging unsaturated moisture flow in cement-based materials with discrete cracks? *Cement and Concrete Research* 91: 61–72.

Sohn H, Park G, Wait JR, Limback NP and Farrar CR (2003) Wavelet-based active sensing for delamination detection in composite structures. *Smart Materials and structures* 13(1): 153.

Somersalo E, Cheney M and Isaacson D (1992) Existence and uniqueness for electrode models for electric current computed tomography. *SIAM Jour. on Appl. Math.* 52(4): 1023–1040.

Surana KS and Reddy J (2016) *The Finite Element Method for Boundary Value Problems: Mathematics and Computations*. CRC Press.

Tallman T, Gungor S, Koo G and Bakis C (2017) On the inverse determination of displacements, strains, and stresses in a carbon nanofiber/polyurethane nanocomposite from conductivity data obtained via electrical impedance tomography. *Journal of Intelligent Material Systems and Structures* : 1–13.

Tallman T and Hernandez J (2017) The effect of error and regularization norms on strain and damage identification via electrical impedance tomography in piezoresistive nanocomposites. *NDT & E International* 91: 156–163.

Tallman TN, Gungor S, Wang K and Bakis CE (2015) Damage detection via electrical impedance tomography in glass fiber/epoxy laminates with carbon black filler. *Structural Health Monitoring* 14(1): 100–109.

Tamburrino A and Rubinacci G (2002) A new non-iterative inversion method for electrical resistance tomography. *Inverse Problems* 18(6): 1809.

Tamburrino A, Rubinacci G, Soleimani M and Lionheart W (2003) A noniterative inversion method for electrical resistance, capacitance and inductance tomography for two phase materials. In: *Proc. 3rd World Congress on Industrial Process Tomography, Canada*. pp. 233–238.

Vauhkonen M, Lionheart W, Heikkinen L, Vauhkonen P and Kaipio J (2001) A MATLAB package for the EIDORS project to reconstruct two-dimensional EIT images. *Physiol. Meas.* 22: 107–111.

Vauhkonen PJ, Vauhkonen M, Savolainen T and Kaipio JP (1999) Three-dimensional electrical impedance tomography based on the complete electrode model. *IEEE T. Biomedical Eng.* 46(9): 1150–1160.

Vilhunen T, Kaipio J, Vauhkonen P, Savolainen T and Vauhkonen M (2002) Simultaneous reconstruction of electrode contact impedances and internal electrical properties: I. theory. *Measurement Science and Technology* 13(12): 1848.

Vogel CR and Oman ME (1996) Iterative methods for total variation denoising. *SIAM Journal on Scientific Computing* 17(1): 227–238.

Wang L and Chan TH (2009) Review of vibration-based damage detection and condition assessment of bridge structures using structural health monitoring. QUT Conference Proceedings.

Ward KM, Zandt G, Beck SL, Christensen DH and McFarlin H (2014) Seismic imaging of the magmatic underpinnings beneath the altiplano-puna volcanic complex from the joint inversion of surface wave dispersion and receiver functions. *Earth and Planetary Science Letters* 404: 43–53.

Yang Y, Sun P, Nagarajaiah S, Bachilo SM and Weisman RB (2017) Full-field, high-spatial-resolution detection of local structural damage from low-resolution random strain field measurements. *Journal of Sound and Vibration* 399: 75–85.

Yao Y, Tung STE and Glisic B (2014) Crack detection and characterization techniques—an overview. *Structural Control and Health Monitoring* 21(12): 1387–1413.

Zalameda JN, Burke ER, Horne MR and Madaras EI (2017) Large area nondestructive evaluation of a fatigue loaded composite structure. In: *Residual Stress, Thermomechanics & Infrared Imaging, Hybrid Techniques and Inverse Problems, Volume 9*. Springer, pp. 21–28.

Zhang Z, Shankar K, Ray T, Morozov EV and Tahtali M (2013) Vibration-based inverse algorithms for detection of delamination in composites. *Composite Structures* 102: 226–236.